A&A 614, A78 (2018)
https://doi.org/10.1051/0004-6361/201731945

Astronomy & Astrophysics

Simulation of the small-scale magnetism in main-sequence stellar atmospheres

R. G. Salhab[1], O. Steiner[1,2], S. V. Berdyugina[1], B. Freytag[3], S. P. Rajaguru[4], and M. Steffen[5]

[1] Kiepenheuer-Institut für Sonnenphysik, Schöneckstraße 6, 79104 Freiburg, Germany
e-mail: salhab@leibniz-kis.de;steiner@leibniz-kis.de
[2] Istituto Ricerche Solari Locarno (IRSOL), Via Patocchi 57–Prato Pernice, 6605 Locarno-Monti, Switzerland
[3] Department of Physics and Astronomy, Uppsala University, Box 516, 751 20 Uppsala, Sweden
[4] Indian Institute of Astrophysics, Koramangala II Block, Bangalore 560 034, India
[5] Leibniz-Institut für Astrophysik (AIP), An der Sternwarte 16, 14482 Potsdam, Germany

Received 13 September 2017 / Accepted 25 January 2018

ABSTRACT

Context. Observations of the Sun tell us that its granular and subgranular small-scale magnetism has significant consequences for global quantities such as the total solar irradiance or convective blueshift of spectral lines.
Aims. In this paper, properties of the small-scale magnetism of four cool stellar atmospheres, including the Sun, are investigated, and in particular its effects on the radiative intensity and flux.
Methods. We carried out three-dimensional radiation magnetohydrodynamic simulations with the CO^{5}BOLD code in two different settings: with and without a magnetic field. These are thought to represent states of high and low small-scale magnetic activity of a stellar magnetic cycle.
Results. We find that the presence of small-scale magnetism increases the bolometric intensity and flux in all investigated models. The surplus in radiative flux of the magnetic over the magnetic field-free atmosphere increases with increasing effective temperature, $T_{\rm eff}$, from 0.47% for spectral type K8V to 1.05% for the solar model, but decreases for higher effective temperatures than solar. The degree of evacuation of the magnetic flux concentrations monotonically increases with $T_{\rm eff}$ as does their depression of the visible optical surface, that is the Wilson depression. Nevertheless, the strength of the field concentrations on this surface stays remarkably unchanged at ≈1560 G throughout the considered range of spectral types. With respect to the surrounding gas pressure, the field strength is close to (thermal) equipartition for the Sun and spectral type F5V but is clearly sub-equipartition for K2V and more so for K8V. The magnetic flux concentrations appear most conspicuous for model K2V owing to their high brightness contrast.
Conclusions. For mean magnetic flux densities of approximately 50 G, we expect the small-scale magnetism of stars in the spectral range from F5V to K8V to produce a positive contribution to their bolometric luminosity. The modulation seems to be most effective for early G-type stars.

Key words. stars: atmospheres – stars: magnetic field – stars: activity – magnetohydrodynamics (MHD) – Sun: atmosphere – Sun: magnetic fields

1. Introduction

Like the Sun, virtually every cool star exhibits magnetic activity. This magnetic activity is observable, for example, as X-ray and chromospheric emissions, as light-curve variability owing to starspots or flares, or by direct magnetic field measurements (for reviews see, e.g., Pagano et al. 2006; Donati & Landstreet 2009; Reiners 2012; Giampapa 2016; Kochukhov et al. 2017). Such activity is mostly due to the large-scale magnetism as found in active regions on the Sun, which harbor large-scale magnetic flux concentrations in the form of sunspots. The effects of small-scale magnetic flux concentrations, as occurring on the Sun in the neighborhood of sunspots, in ephemeral active regions but also outside of active regions, are less accessible in the case of stellar atmospheres. We know little about their stellar existence and about their physical constitution in function of stellar spectral type.

From observations of the Sun, it is well established that small magnetic flux concentrations, often referred to as magnetic elements, exist. These magnetic elements preferentially reside in intergranular space and have a typical horizontal size of 100 km. They appear in white-light images of the Sun as a bright structure, not dark like sunspots. The larger of these magnetic flux concentrations appear in the form of (bright) faculae, when located near the limb of the solar disk. On a sufficiently long timescale (of months), their bolometric brightness overcompensates the lack of radiation from dark sunspots (Shapiro et al. 2016). In response, the total solar irradiance (TSI) is slightly larger at times of high magnetic activity (solar maximum) than at times of a solar minimum when there are fewer magnetic elements present on the solar disk (Fröhlich 2013). Hence, the variation of the TSI with the solar cycle, which is approximately 0.1%, is an important global manifestation of the small-scale magnetism of the Sun. Local enhancements of small-scale magnetism may impede convective motions at the solar surface, which reduces the convective blueshift of spectral lines that naturally results from granulation. Depending on the presence or scarcity of small-scale magnetism over the course of the solar cycle, this then results in a variation of the disk-integrated convective blueshift and bisector shape of spectral lines as another global manifestation of small-scale magnetism (Meunier et al. 2010; Haywood et al. 2016).

It is clear that these global effects must also be observable in the case of solar-like stars, for example, in the form of a dependence of the photometric luminosity or measured radial velocity on the phase of the stellar magnetic cycle. For solar twins, this relationship can be expected to behave like on the Sun but it does not need to be a priori solar-like for other stellar atmospheres. From a 13–20 yr time series of 32 primarily main-sequence Sun-like stars, Lockwood et al. (2007) have concluded that on a year-to-year timescale, young active stars become fainter when their Ca II emission (which is a measure of magnetic activity) increases, while older, less active stars such as the Sun become brighter when their Ca II emission increases. The magnetically modulated photometric variability and radial velocity, and their modeling, are of considerable interest for exoplanet detection and characterization.

Questions regarding the relationships between small-scale magnetism and global quantities (such as photometric luminosity or radial velocity) in dependence on the stellar spectral type, can be addressed with the help of three-dimensional, dynamical, numerical simulations of stellar atmospheres of varying spectral types. Applied to the Sun, these kind of simulations have achieved a degree of realism that provides confidence in applying them to solar-like stellar atmospheres as well.

Three-dimensional, realistic numerical simulations of convective flow and overshoot in the near surface layers of stellar atmospheres have first been carried out by Atroshchenko et al. (1989a,b), Nordlund & Dravins (1990), and Dravins & Nordlund (1990a,b). More recently, these early attempts have culminated in the establishment of grids of three-dimensional stellar model atmospheres such as the CIFIST grid (Ludwig et al. 2009; Tremblay et al. 2013), the grid of Trampedach et al. (2013), the STAGGER grid (Magic et al. 2013a,b), the grid of Tanner et al. (2013), or the sequence of six representative stellar models along the cool main-sequence branch by Beeck et al. (2013a,b).

Corresponding three-dimensional stellar atmospheric simulations that include magnetic fields are still rare, unlike the case of solar magnetohydrodynamic (MHD) models. This state of affairs is certainly owed to the fact that small-scale magnetic fields on the Sun can be detected and measured in great detail and with high precision, while this is not possible for stars. Beeck et al. (2011) reported on MHD simulations, starting from the same six models mentioned above but introducing initial homogeneous vertical magnetic fields with strengths of 20 G, 100 G, and 500 G. These authors found distinctive differences between solar-like small-scale magnetic structures and those forming in M dwarfs, where the latter are more pore-like. Steiner et al. (2014) analyzed MHD models of spectral types K8V to F5V[1], concluding that the field strength of the strongest flux concentrations (i) was fairly independent of spectral type when measured at the optical depth level $\tau_R = 1$; (ii) assumed thermal superequipartition for the Sun and warmer atmosphere, while staying much weaker for cool atmospheres; and (iii) that their presence correlates with enhanced bolometric radiative intensity and flux.

Beeck et al. (2015a,b) thoroughly analyzed their main-sequence models of spectral types M2V to F3V and of various initial magnetic field strengths and, inter alia, confirmed the findings (i) to (iii), extending their validity to a wider range of spectral types and magnetic fluxes. Furthermore, these authors found that M dwarfs lack bright magnetic structures in unipolar regions of moderate field strength and that the spatial correlation between velocity and the magnetic field varies significantly along the model sequence. The presence, abundance, and strength of the small-scale magnetic fields impact the local thermodynamical structure and the flow field and thus influence substantially the measurement of global magnetic field properties and stellar parameters.

In this paper, we present simulations and their analysis of the same spectral sequence that was considered in the preliminary study of Steiner et al. (2014) but now augmented by equivalent comparison runs without magnetic field and for a much longer simulation time for improving reliability. A central question to be answered is whether and to what extent the presence of small-scale magnetism enhances radiative loss from stellar surfaces other than the Sun. Quantitative results are all summarized in Table 2 to which we refer throughout the paper. In Sect. 2, we present characteristics of the four simulation runs considered (Table 1) and give some basic, mostly radiative properties of the granulation and magnetic flux concentrations in Sect. 3. Section 4 deals with the magnetic field itself before turning to the main topic in Sect. 5, which deals with the question how small-scale magnetism affects the bolometric brightness of the models. Section 6 concentrates on the physical nature of the magnetic flux concentrations, still in dependence on the spectral type, and Sect. 7 discusses the results in comparison to observations and results from previous work and discusses the fundamental assumption of the constant deep adiabat. Conclusions are given in Sect. 8.

2. Models and simulations

We carried out box in a star numerical simulations of the near surface layers of four different cool stellar models. The overall governing parameters in these simulations are the effective temperature, $T_{\rm eff}$, gravitational acceleration, g, and chemical composition. For the latter, we used solar abundances for all models. The nominal effective temperatures of the four models are $T^*_{\rm eff}$ = 4000 K (K8V), 5000 K (K2V), 5770 K (G2V, solar), and 6500 K (F5V). The gravitational acceleration, which is that at the stellar surface, is $\log g = 4.5$ for all models except the solar model for which the actual solar value of $\log g = 4.44$ was taken. The approximate spectral types corresponding to these fundamental parameters were determined according to Gray & Corbally (2008).

For each of these model atmospheres, we carried out two separate simulations: one without magnetic field and one with an initial homogeneous magnetic field of 50 G strength. The value of 50 G may be a realistic value for the mean magnetic flux in a predominantly unipolar region of the quiet Sun and it is about what is expected for the turbulent magnetic field of a quiet region of mixed polarities (Faurobert-Scholl 1993; Trujillo Bueno et al. 2004). Values for corresponding quiet stellar regions are not known but we used the same solar values as a first guess and for ease of comparison.

2.1. Simulations

The simulation of the three-dimensional, time-dependent, non-stationary stellar atmospheres involves the solution of the time-dependent system of MHD equations for a compressible, partially ionized plasma, taking radiative transfer into account. The simulations were performed with the CO^{5}BOLD code (Freytag et al. 2012). The three-dimensional computational domain has periodic lateral boundary conditions and open top

[1] The effective temperatures of the sequence in Steiner et al. (2014) was the same as investigated in the present paper but the assignment of spectral types was different. We refer to these models with the classification as given in Table 1.

and bottom boundaries in the sense that the plasma can freely flow across these boundaries under the condition of vanishing net mass flux at the bottom. The specific entropy of the mass that flows into the physical domain across the bottom boundary was set to a fixed value. This value was obtained from previous simulation runs during which it was adjusted so as to yield a radiative flux at the top boundary that closely matches the specified nominal effective temperature $T_{\rm eff}^{*}$. The magnetic field is kept vertical at the bottom and top boundary, but it can freely move in lateral directions. For a reliable comparison of the pair of runs with and without magnetic field, we used for both runs the same MHDs module of CO^{5}BOLD, which uses a HLL Harten et al. 1983 approximate Riemann solver (see Freytag et al. 2012) and the WENO-type (weighted essentially non-oscillatory) reconstruction scheme FRWENO of Freytag (2013). All numerical parameters and boundary conditions are kept exactly the same in both runs.

We carried out the radiation transfer with a modified Feautrier scheme based on long characteristics as described in more detail in Freytag et al. (2012).

While the azimuthal angle is restricted to 0, $(1/2)\pi$, π, and $(3/2)\pi$, two non-zero inclination angles per quadrant were used for the altitude in addition to the vertical ray direction according to Lobatto's quadrature formula (Davis & Polonsky 1972).

To account for the frequency dependence of the radiative transfer, we used a multigroup technique, in which opacities of similar strengths are sorted into a small number of opacity bins. Within each opacity bin, an average opacity is computed as a depth-dependent combination of Planck and Rosseland mean over the bin, except for bin 5 (strongest opacities), which is a Rosseland mean. The monochromatic opacities entering the opacity binning scheme were adapted from the MARCS stellar atmosphere package (Gustafsson et al. 2008) and were kindly provided by B. Plez (priv. comm.). The radiative transfer of the present simulations uses five opacity bins. The equation of state accounts for the ionization balance of HI, HII, H2, HeI, HeII, HeIII, and a representative metal. Pre-tabulated values of gas pressure, temperature, and thermodynamic derivatives as functions of density and internal energy are used.

2.2. The physical domain

The physical size and scale of the simulation boxes are given in Table 1. The parameter $H_{\rm p}(\tau_{\rm R}=1)$ is the pressure scale height spatially and temporally averaged over the surface of Rosseland optical depth $\tau_{\rm R}=1$ and the simulated physical time. This value increases with increasing effective temperature because $H_{\rm p}$ is proportional to the local temperature. The Sun is an exception here because it has a surface gravity that is 13% less than that of the other models. The height extent of the boxes above and below the mean optical depth $\tau_{\rm R}=1$ is given in km and in terms of pressure scale heights, with

$$N_{H_{\rm p}}(\tau_{\rm R}\geq 1)=\ln(p_{\rm bot}/p_0) \quad \text{and} \quad N_{H_{\rm p}}(\tau_{\rm R}\leq 1)=\ln(p_0/p_{\rm top}), \tag{1}$$

where $p_{\rm top}$ and $p_{\rm bot}$ are the mean gas pressures at the top and bottom of the box, respectively, and p_0 is the mean gas pressure at z_0, which is the spatial and temporal average height of the $\tau_{\rm R}=1$ level, i.e., $z_0=\langle z(\tau_{\rm R}=1)\rangle$. Vertically, the boxes extend over about 11–14 pressure scale heights. The heights of the computational cells, Δz, are chosen such that the pressure scale height at the mean $\tau R=1$-level is resolved by about 12 cells. The value Δz is kept constant over the entire height extent of the computational domain.

Table 1. Basic properties of the simulation models.

Spectral type	K8V	K2V	G2V	F5V
$T_{\rm eff}^{*}$ [K] (nominal)	4000	5000	5770	6500
$\log g$	4.5	4.5	4.44	4.5
$H_{\rm p}(\tau_{\rm R}=1)$ [km]^a	88.1	112.4	149.1	143.2
Box depth [km]				
Below $\tau_{\rm R}=1$	744	1785	1333	3413
Above $\tau_{\rm R}=1$	482	690	911	592
Box depth [$N_{H_{\rm p}}$]^b				
Below $\tau_{\rm R}=1$	3.88	5.79	3.85	6.54
Above $\tau_{\rm R}=1$	6.86	8.32	7.93	4.94
Box width [km]	4734	4928	5600	8388
Δz [km]	7	9	12	15
$H_{\rm p}(\tau_{\rm R}=1)/\Delta z$	12.6	12.5	12.4	9.5
$\Delta x, \Delta y$ [km]	9	11	14	18
$L_{\rm gran}$ [km]	468	588	772	910
$L_{\rm gran}/\Delta x$	54	53	55	51
Box width [$N_{L_{\rm gran}}$]	10.1	8.4	7.3	9.2
$N_{x,y}$	526	448	400	466
N_z	176	276	188	268
$t_{\rm start}$ [min]	33	33	33	33
$t_{\rm end}$ [min]	666	666	666	666
$t_{\rm run}$ [min]	633	633	633	633

Notes. See text in Sect. 2 for more details. For each spectral type two runs were carried out: one without a magnetic field and one with an initial homogeneous vertical field of a flux density of 50 G. Where not univocal, data refer to the magnetic field-free simulation. $^{(a)}H_{\rm p}$ is the pressure scale height. $^{(b)}N_{H_{\rm p}}$ is the number of pressure scale heights.

The horizontal extent of the boxes increases with effective temperature in accordance with the average size of the granules, which increase as well. Both quantities are also listed in Table 1; i.e., the average size of granules in kilometers and number of computational cell widths, Δx, and the horizontal extent of the box in kilometers and number of granular scales, $L_{\rm gran}$. From these numbers we see that for all models, the average granular scale is resolved by 50–55 computational cells. Here, the granular scale is computed from

$$L_{\rm gran}=\langle 2\sqrt{A/\pi}\rangle, \tag{2}$$

where A is the average surface area of the granules. The surface areas of granules is determined by first searching for the areas of positive vertical velocities (upflows) at $z=z_0$, followed by the application of a connected-component labeling algorithm (Wu et al. 2009). This also includes poorly developed or vanishing granules. By this definition, the box sizes are between $N_{L_{\rm gran}}=7$ and 10 mean granular scales. At any time, there are about 12–25 well-developed granules within the field of view. These dimensions and spatial resolutions result in boxes of roughly $500\times500\times250$ computational cells. The precise numbers are given in Table 1.

The simulations were started from previously existing relaxed non-magnetic models of coarser spatial resolution. These models were then regridded to the present higher resolution boxes and run for 40 000 s, i.e., ≈11 h physical time. The starting point for the analysis is 2000 s after the regridding. In the case of simulations with a magnetic field, they were started from a snapshot of the corresponding evolved non-magnetic simulation to which the field was inserted and run for 2000 s before starting the analysis. The concentration to kG magnetic fields from

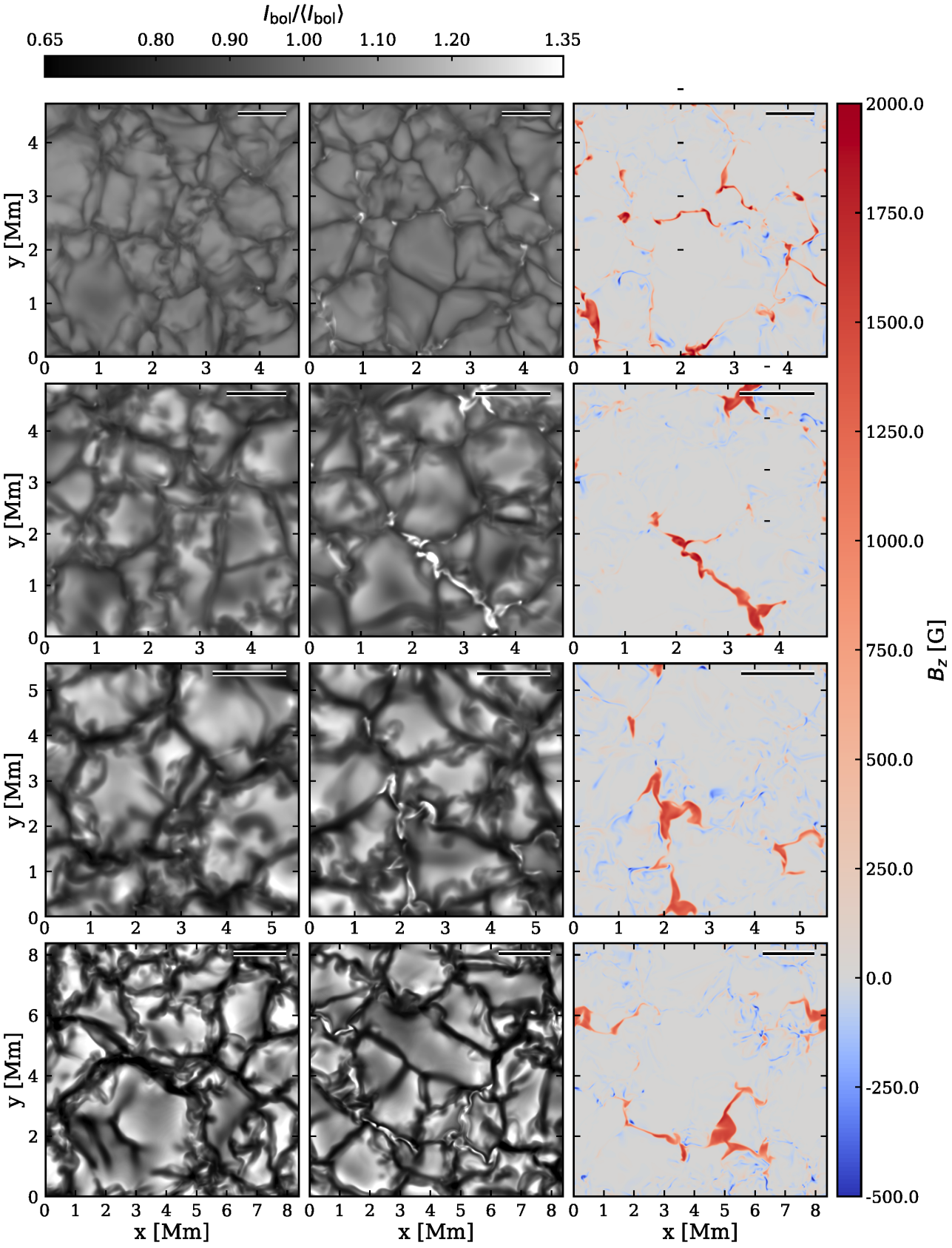

Fig. 1. Representative time instants of the vertically directed bolometric radiation of the non-magnetic simulations (*left column*) and of the magnetic simulations (*middle column*), normalized to their respective mean intensities. In the *right column* are the corresponding time instants of the vertical magnetic field strength at depth $z_0 = \langle z(\tau_R = 1)\rangle$. Rows from *top* to *bottom* correspond to the spectral types K8V, K2V, G2V, and F5V, respectively. The snapshots of the bolometric intensities are saturated at $I_{bol}/\langle I_{bol}\rangle = 0.65$ and 1.35. The black bar on white background in the top right corner of each panel has a length of $10 \times H_p(z_0)$.

Table 2. Properties of the four spectral types of dynamical non-magnetic and magnetic stellar atmospheres.

	Spectral type	K8V		K2V		G2V		F5V	
	initial B_z [G]	0	50	0	50	0	50	0	50
1	rms($B_{z\,\mathrm{MBF}}(z_0)$) [G]		1438 ± 40		1348 ± 42		1282 ± 40		1248 ± 32
2	rms($B_{z\,\mathrm{MBF}}(\tau_\mathrm{R}=1)$) [G]		1575 ± 53		1598 ± 93		1480 ± 84		1565 ± 81
3	max($\lvert B_{z\,\mathrm{MBF}}(z_0)\rvert$) [G]		2204 ± 79		1871 ± 63		1739 ± 73		1675 ± 85
4	max($\lvert B_{z\,\mathrm{MBF}}(\tau_\mathrm{R}=1)\rvert$) [G]		2872 ± 175		2771 ± 191		2616 ± 248		3134 ± 334
5	$B_{z\,\mathrm{strong}}(z_0)$ [G]		1621 ± 230		1555 ± 136		1416 ± 146		1372 ± 135
6	$B_{z\,\mathrm{strong}}(\tau_\mathrm{R}=1)$ [G]		1800 ± 407		1951 ± 368		1660 ± 467		1754 ± 651
7	rms($B_z(z_0)$) [G]		249.9 ± 5.5		248.0 ± 8.0		238.3 ± 7.2		237.9 ± 6.5
8	$p_\mathrm{gas}(z_0)$ [kPa]	26.5 ± 0.1	26.9 ± 0.1	14.9 ± 0.1	15.2 ± 0.1	10.2 ± 0.1	10.5 ± 0.2	7.34 ± 0.1	7.52 ± 0.2
9	$p_\mathrm{mag}(z_0)$ [kPa]		8.2 ± 0.5		7.3 ± 0.5		6.5 ± 0.5		6.2 ± 0.3
10	$p_\mathrm{dyn}(z_0)$ [kPa]	2.3 ± 0.2	1.8 ± 0.1	1.9 ± 0.1	1.7 ± 0.1	2.2 ± 0.1	2.0 ± 0.1	2.3 ± 0.1	2.2 ± 0.1
11	$p_\mathrm{tot}(z_0)$ [kPa]	28.8 ± 0.1	28.6 ± 0.1	16.7 ± 0.1	16.9 ± 0.1	12.4 ± 0.1	12.5 ± 0.2	9.68 ± 0.1	9.66 ± 0.2
12	$B_{\mathrm{eq\ th}}(z_0)$ [G]	2574 ± 5	2596 ± 5	1929 ± 5	1951 ± 7	1594 ± 11	1614 ± 12	1345 ± 13	1362 ± 15
13	$B_{\mathrm{eq\ dyn}}(z_0)$ [G]	710 ± 26	629 ± 18	641 ± 24	617 ± 18	703 ± 21	674 ± 20	720 ± 19	696 ± 17
14	$B_{\mathrm{eq\ tot}}(z_0)$ [G]	2685 ± 4	2681 ± 5	2048 ± 5	2058 ± 7	1762 ± 10	1765 ± 11	1552 ± 11	1550 ± 13
15	$\rho_\mathrm{int}/\rho_\mathrm{ext}(z_0)$ [–]		0.75 ± 0.02		0.54 ± 0.03		0.46 ± 0.04		0.36 ± 0.05
16	$\beta(z_0)$ [–]		2.7 ± 0.2		1.3 ± 0.1		0.74 ± 0.1		0.38 ± 0.1
17	T_eff (actual) [K]	3976 ± 4	3981 ± 3	4957 ± 8	4968 ± 11	5761 ± 14	5775 ± 16	6434 ± 13	6447 ± 14
18	$I_{\mathrm{bol}\,0}$ [erg cm^{-2} s^{-1} sr^{-1}]	5.15×10^9		1.32×10^{10}		2.38×10^{10}		3.65×10^{10}	
19	$F_{\mathrm{bol}\,0}$ [erg cm^{-2} s^{-1}]	1.42×10^{10}		3.42×10^{10}		6.25×10^{10}		9.71×10^{10}	
20	$\langle I_\mathrm{bol}\rangle/\langle I_{\mathrm{bol}\,0\,\mathrm{sun}}\rangle$ [–]	0.22	0.22	0.56	0.56	1.0	1.01	1.53	1.54
21	c_rms [%]	5.6 ± 0.1	5.5 ± 0.1	9.8 ± 0.3	10.4 ± 0.3	15.3 ± 0.5	14.9 ± 0.5	18.7 ± 0.3	18.4 ± 0.3
22	$c_{\mathrm{MBF\,rms}}$ [%]		9.3 ± 1.4		25.6 ± 3.0		18.7 ± 2.9		18.8 ± 1.5
23	$c_{\mathrm{MBF\,max}}$ [%]		49 ± 11		86 ± 12		72 ± 12		61 ± 16
24	$c_{\mathrm{MBF-gran}}$ [%]		0.43 ± 1.3		14.2 ± 3.1		0.56 ± 3.4		−7.8 ± 3.1
25	δ_{I_bol} [%]	0.30 ± 0.4 ± 0.03		0.65 ± 1.1 ± 0.03		0.79 ± 1.5 ± 0.06		0.43 ± 1.2 ± 0.06	
26	δ_{F_bol} [%]	0.47 ± 0.5 ± 0.04		0.85 ± 1.1 ± 0.03		1.02 ± 1.5 ± 0.07		0.82 ± 1.2 ± 0.06	
27	$\delta_{F_\mathrm{bol}} - \delta_{I_\mathrm{bol}}$ [%]	0.17		0.20		0.23		0.39	
28	WD [km]		46 ± 16		94 ± 37		160 ± 60		231 ± 108
29	WD/$H_p(\tau_R=1)$ [–]		0.5 ± 0.2		0.8 ± 0.3		1.1 ± 0.4		1.6 ± 0.8
30	$\mathrm{WD_w}$ [km]		60 ± 14		139 ± 34		232 ± 65		388 ± 113
31	$\mathrm{WD_w}/H_p(\tau_R=1)$ [–]		0.7 ± 0.2		1.2 ± 0.3		1.6 ± 0.4		2.7 ± 0.8
32	$A_\mathrm{MBF}/A_\mathrm{total}$ [%]		2.17 ± 0.07		2.29 ± 0.11		2.03 ± 0.18		2.17 ± 0.12
33	$A_\mathrm{gran}/A_\mathrm{total}$ [%]	56.4 ± 1.8	57.7 ± 1.2	53.0 ± 1.8	52.9 ± 1.3	55.0 ± 2.5	54.8 ± 2.4	57.3 ± 1.9	56.2 ± 1.7

Notes. Indicated scatter is the 1σ deviation in the temporal fluctuation of the quantities. For the precise definition of the quantities, see text (Sects. 3–7) and formulas. For their derivation, data of the full simulation time of 38 000 s with a cadence of 250 s were used, except for rows 17–21 and 25–27 for which the cadence was 10 s.

the initial homogeneous 50 G field takes only a few minutes for each model. Every 10 s, spatially averaged data and the intensity of the vertically directed radiation that leaves the box from the top boundary in each opacity band were stored. This then is the cadence for the analyses that are based on the radiative quantities alone. The full box with mass density, internal energy, velocity field, and magnetic field for every grid cell are stored every 250 s. Analyses that require detailed information about the spatial distribution of the magnetic field, such as those that are based on the masking of magnetic elements, have that cadence.

3. Characteristics of the granulation and the magnetic filigree

Before studying the details of the small-scale magnetism and the radiative implications of it, we provide an overview on some basic properties of the four different stellar model atmospheres. A compilation of arbitrary time instances of the simulations is given in Fig. 1, from the coolest model, K8V, in the top row to the warmest model, F5V, in the bottom row. Table 2 gives the physical quantities that result from the simulations. The entries in Table 2 are explained in detail in this and following sections. The left column of Fig. 1 shows the intensity of the vertically directed bolometric radiation that leaves the box through the top boundary of the non-magnetic models. The middle column shows the intensity for the corresponding magnetic runs. As we know from the Sun, the visible surface structure in all panels consist of bright granules, in which plasma rises to the surface, and dark intergranular lanes, where plasma flows back into the star.

3.1. Characteristics of the granulation

First, we noticed that the intensity contrast between granules and intergranular lanes drastically increases from the coolest to warmest model and substructure of granules and the intergranular space becomes increasingly visible. To highlight this well-known behavior, the same grayscale range is applied for all the intensity maps of Fig. 1. It can be quantified with the time

averaged root mean square (rms) of the intensity contrast, given as

$$c_{\rm rms} = \left\langle \sqrt{\left\langle \left(\frac{I_{\rm bol} - \langle I_{\rm bol}\rangle}{\langle I_{\rm bol}\rangle} \right)^2 \right\rangle} \right\rangle_t , \tag{3}$$

where $\langle \cdots \rangle$ symbolizes the average over the full intensity map of a simulation instant, $\langle \cdots \rangle_t$ the average over time, and $I_{\rm bol}$ the intensity of the vertically directed bolometric radiation in a single pixel. From row 21 of Table 2, one can see that this value increases from 5.6% for K8V to 18.7% for F5V for the non-magnetic models, while the solar model has 15.3% and 14.9% for the non-magnetic and magnetic model, respectively. These solar values are in line with rms continuum contrasts of 14–15% at 630 nm of a simulation assisted reconstruction by Danilovic et al. (2008) derived from disk-center intensity maps obtained with the spectropolarimeter (SP) of the Hinode Solar Optical Telescope (SOT), which gave an original contrast of 7% at 630 nm. Wedemeyer-Böhm & Rouppe van der Voort (2009) obtained a value of (16.6 ± 0.7)% from the original (6.2 ± 0.2)% measured in the red bandpass (centered at 668.40 nm) with the Broadband Filter Instrument (BFI) of SOT/Hinode after deconvolution with the appropriate optical transfer function of the telescope. The magnetic models have, with the exception of K2V, slightly smaller rms contrasts because part of the intergranular lanes is filled with bright magnetic features that are similarly bright as the granules. Our contrast values are also in satisfactory agreement with those of Magic et al. (2013a, their Appendix C) obtained with a different simulation code. We tend to get higher contrast values for models K2V and G2V (9.8 vs. 8.8% and 15.3 vs. 14.6%, respectively) but the agreement is perfect for model F5V.

The strong increase of the rms granular intensity contrast with increasing effective temperature can be understood when examining the relative temperature fluctuation as a function of optical depth for the various spectral types as in Beeck et al. (2013a). The rms of the relative temperature fluctuations for the present four spectral types are shown in Fig. 2[2]. We see that the fluctuation at the visible optical surface, $\log\tau = 0$, increase from 1.9% for K8V to 4.9% for F5V, which explains the increase in rms intensity contrast. The peak fluctuations increase from 4% for K8V to 8.7% for F5V, which is because with increasing effective temperature, the energy throughput increases and the convective dynamics become more vigorous. Also, the increase of the fluctuations with optical depth is less steep for the spectral type K8V than for the warmer types, which is due to the lower temperature sensitivity of the opacity for the plasma in the state that prevails around $\log\tau = 0$ of cooler (K and M) stars compared to earlier spectral types. Correspondingly, the temperature fluctuations tend to become hidden from view in the case of K8V, while it is more pronounced closely beneath the visible surface in the case of F5V. Therefore, granules of atmospheres cooler than about K5V are known as veiled granules (low rms contrast) and granules of warmer atmospheres are known as naked granules (high rms contrast; Nordlund & Dravins 1990; Magic et al. 2013a; Beeck et al. 2013a,b).

While differences in the temperature fluctuations are vanishingly small between the magnetic and the non-magnetic models below $\tau = 1$, these fluctuations are systematically higher for the magnetic models in the deep photosphere, where the hot walls (see Sect. 6.2) of the magnetic flux concentrations add to the fluctuations. Higher up in the photosphere, the amplification of waves traveling into the rarefied atmosphere and the formation of shock waves increase the temperature fluctuations of preferentially the magnetic field-free atmosphere, while hydrodynamic waves and shocks tend to become suppressed by the stiffening effect of the magnetic field in the magnetic atmosphere.

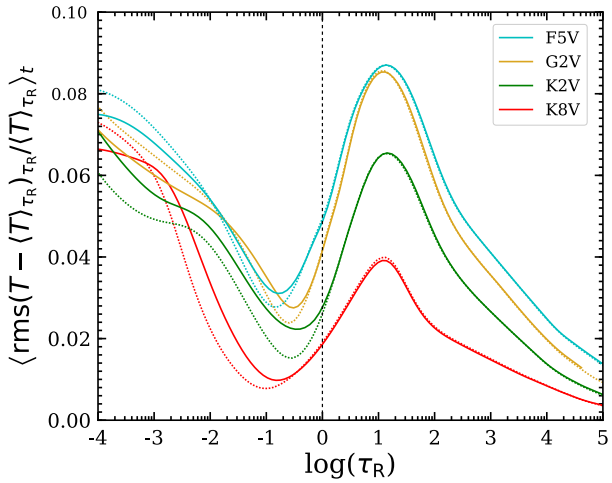

Fig. 2. Root mean square of the relative temperature fluctuation over iso-$\tau_{\rm R}$ surfaces as a function of Rosseland optical depth, $\tau_{\rm R}$ of the four models of different spectral types. Solid curves refer to the magnetic models, dotted curves to the field-free models. The rms is computed as in Eq. (3), where $I_{\rm bol}$ is replaced by the temperature $T(\tau_{\rm R})$.

We also notice tiny bright dots in the intensity maps of the non-magnetic models, such as the dot at $x = 4$ Mm and $y = 1.3$ Mm of model K8V in Fig. 1. These dots occur in all the investigated spectral types, particularly conspicuous and longevous in K2V. These originate from swirling downdrafts, which give rise to non-magnetic bright points (Vögler et al. 2005; Calvo et al. 2016) due to the low pressure at the center of the vortices, which implies a depression of the optical surface to deeper, hotter layers.

Finally, we recall the well-known fact that the size of the granules increases proportional to the pressure scale height, $H_{\rm p}$, which in turn is approximately proportional to the temperature, both for a given, fixed surface gravity. This can be seen from the indicated bar of length $10 \times H_{\rm p}(z_0)$ in the top right corner of each panel in Fig. 1. These bars are about the size of the granules for each model.

3.2. Characteristics of the magnetic filigree

From the middle column of Fig. 1, we see that all the magnetic models show conspicuous, bright features in bolometric intensity, which coincide with concentrations of magnetic fields. These magnetic field concentrations are shown in the right column of Fig. 1[3]. The bright features are well known from the Sun where they are alternatively referred to as magnetic bright points, facular points, magnetic elements, flux sheets, ribbon bands, crinkles, etc., depending on their shape and the context. Broadly, we speak of the magnetic filigree, a term introduced by Dunn & Zirker (1973), or of magnetic bright features (MBF)[4]. From Fig. 1 and corresponding movies, we readily recognize a

[2] When taking instead $\mathrm{rms}(T - \langle T\rangle_{\tau_{\rm R}\,t})_{\tau_{\rm R}\,t}/\langle T\rangle_{\tau_{\rm R}\,t}$ the curves only differ very marginally from those shown in Fig. 2.

[3] The magnetic polarity is predominantly positive because of the initial condition of a homogeneous, unipolar magnetic field.

[4] In the following we use the term *magnetic filigree* for the collectivity of MBFs, while MBF rather refers to structure elements of the filigree.

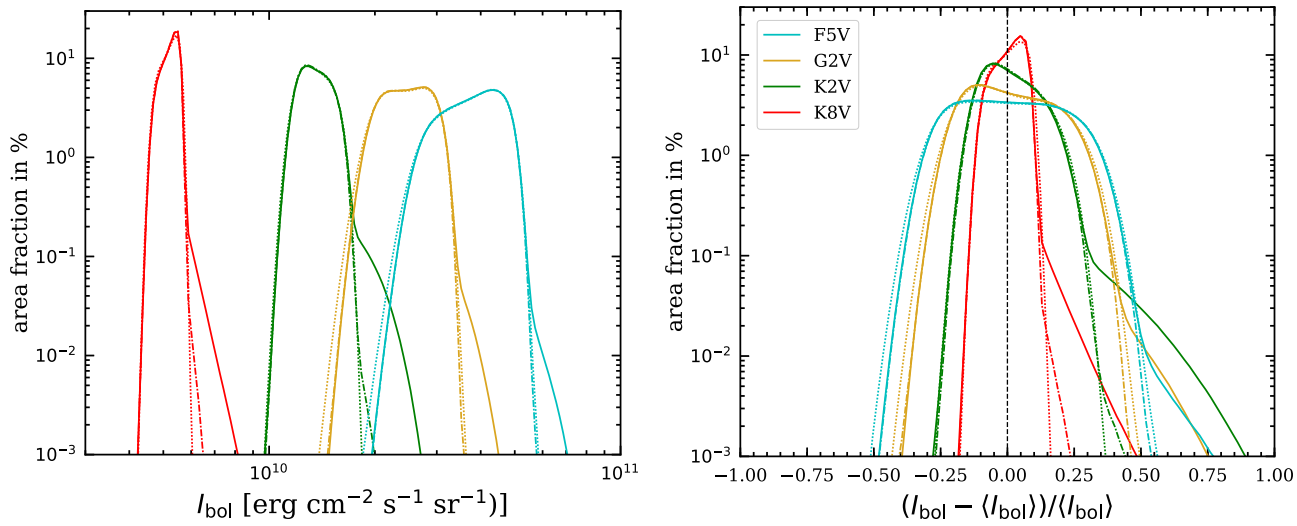

Fig. 3. *Left panel*: histograms of the (logarithmic) bolometric intensity of the vertically directed radiation. The bin size is 0.01 dex. *Right panel*: histograms of the (linear) relative intensity fluctuation. The bin size is 0.02. Solid curves refer to the magnetic models, dotted curves to the field-free models, and the dot-dashed curves to the masked magnetic models for which areas with $B_z(z_0) > 1000$ G are discarded. The color-coded spectral types are indicated in the inset of the panel on the right. The histograms are based on the intensity maps of the full time series.

tendency for the magnetic filigree of the coolest model (K8V) to have a more compact, point-like appearance forming at the vertices of intergranular lanes, while it has a more sheet-like shape in all the other models. This may be because the absolute width of the intergranular space decreases with decreasing effective temperature as can be seen from the rapid decline of L_{gran} (see Table 1), while the relative granular area (row 33 of Table 2) remains almost constant (see also Ludwig et al. 2002; Beeck et al. 2013b). If it is small enough, the formation of magnetic flux sheets between and alongside granule boundaries may be hampered, leaving mainly the vertices of intergranular lanes for magnetic flux concentrations strong enough to become conspicuous in maps of bolometric intensity. But also the fraction of the field of view covered by granules (row 33 of Table 2) is for the magnetic models maximal (58%) for spectral type K8V, while it continuously drops from 57.2 to 53.3% from F5V to K2V, respectively, distinguishing K8V as having relatively narrow intergranular lanes. This behavior and numbers differ from Table 1 of Beeck et al. (2013b), which is probably because of the different determination of the granular area.

Figure 3 shows the histogram of the absolute radiative intensity (left panel) and the histogram of the relative intensity fluctuation (right panel) and in each panel the non-magnetic models (dotted curves) and magnetic models (solid curves). The cooler spectral types have a distinctly narrower distribution of intensities than the warmer spectral types, which simply is expression of the fact that the rms of the relative intensity fluctuation (contrast) increases from 5.6% for K8V to 18.7% for F5V (for the non-magnetic models), as discussed in Sect. 3.1. We also see that the intensity distribution of the magnetic models show a shoulder at the high end of intensities, which is absent in the non-magnetic case. This shoulder is particularly well developed in the case of the model K2V and is due to the magnetic filigree. To verify the latter statement, the intensity histograms were also evaluated for the case in which areas of the magnetic models with a magnetic field strength $B_z(z_0) > 1000$ G were discarded (dot-dashed curves). These histograms show no, or no significant shoulder and look very similar to the intensity distribution of the non-magnetic models, which proves that the magnetic filigree, which becomes masked by the above field-strength criterium, is responsible for the shoulders in all spectral types. We do not find substantial differences in intensities between the magnetic and non-magnetic models in the range of the most frequent intensities nor when examining plots such as Fig. 3 with a linear ordinate axis. A minor exception to this rule is K8V for which the peak occurrence of the magnetic model is slightly higher than that of the non-magnetic model.

At the low end of intensities, the non-magnetic models of the warmer types G2V and F5V tend to have a slightly higher occurrence of dark pixels than the corresponding magnetic models. For models K2V and K8V, this difference almost disappears. This is possibly due to the fraction of integranular space that is filled with MBFs in the magnetic models but remains dark in the non-magnetic case but may also be due to a more fundamental difference in the formation of particularly cool downdrafts that is more developed the earlier the spectral type.

Like Beeck et al. (2013b), Magic et al. (2013a), Trampedach et al. (2013), or Tremblay et al. (2013), we also find signs of a bimodality in the intensity distribution, i.e., a bright and a dark component[5], where the bright component gets steadily weaker relative to the dark component from F5V to K2V but dominates again over the dark component in the model K8V. This change in trend of model K8V is certainly due to the corresponding change in the areal fraction of granules mentioned further above and quantified in row 33 of Table 2. Regarding the distribution of the relative intensity fluctuation (Fig. 3, right panel), the most frequent value is negative for all models but K8V. While the most frequent relative intensity fluctuation of the magnetic model K8V of +5.73% is close to its rms contrast, the most frequent relative intensity excursion for the magnetic models K2V, G2V, and F5V are −5.38, −11.7, and −12.5%, respectively. For the field-free models, these values are a bit less accentuated, being +4.34% for model K8V and −4.24, −10.5, and −10.4% for models K2V, G2V, and F5V, respectively. Consequences of the differences in the intensity distributions between magnetic and non-magnetic models for the mean bolometric intensity and radiative flux is further explored in Sect. 5.

[5] We find this bimodality to be less pronounced with increasing spatial resolution of the simulation, while the rms intensity contrast, c_{rms}, stays constant.

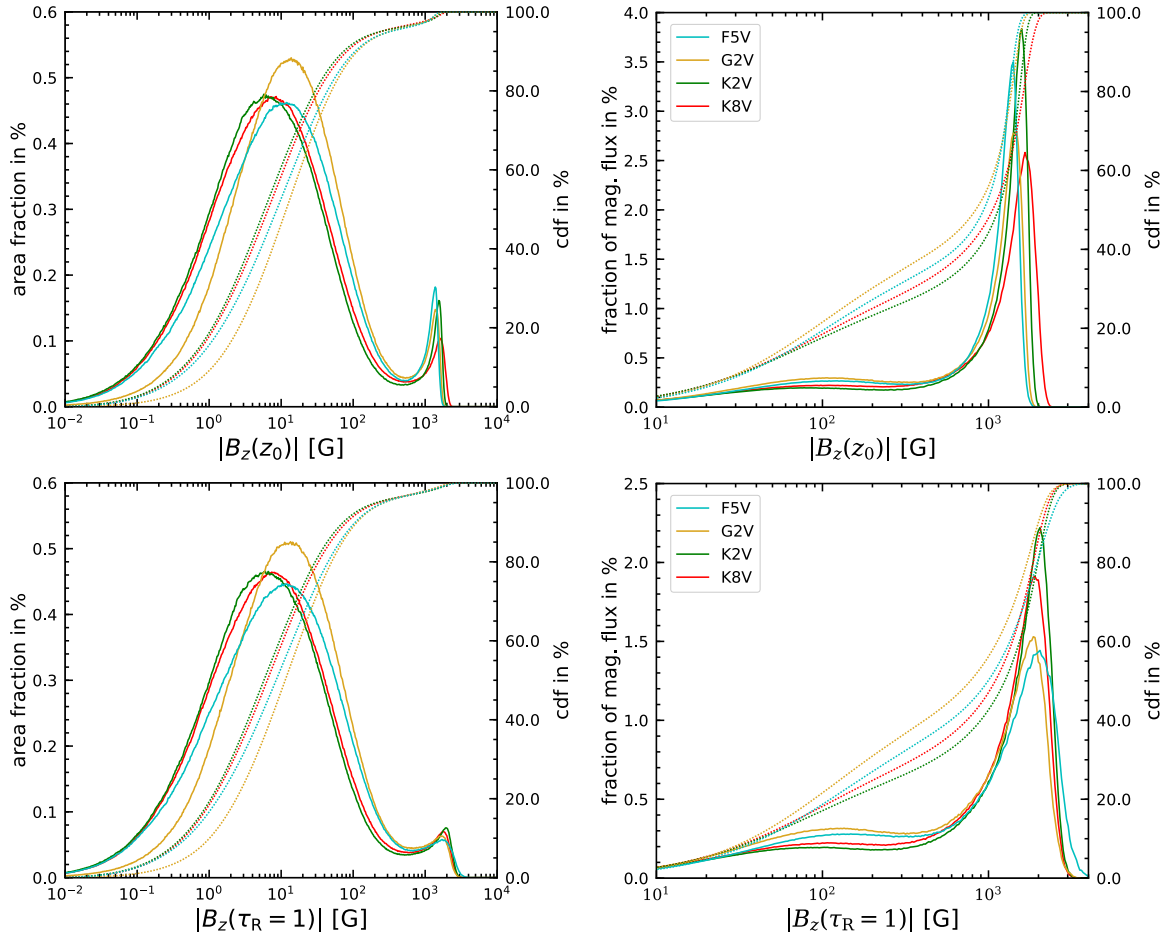

Fig. 4. Histograms (solid curves) of the absolute vertical magnetic field component at the z_0 level (*top*) and on the surface of $\tau_R = 1$ (*bottom*) of the four (color-coded) model atmospheres. The bin size is 0.01 dex. The *panels on the left-hand side* show the area fraction per bin of magnetic field strength. The *panels on the right-hand side* show the fraction of magnetic flux per bin of magnetic field strength. The dotted curves show the cdf with the corresponding ordinate axis on the *right-hand side*. For a given threshold of magnetic field strength, the cdfs indicate the areal fraction (*left panels*) or fraction of magnetic flux (*right panels*) with a strength below that threshold. The histograms are based on the magnetic field maps of the full time series.

4. Characteristics of the magnetic flux concentrations

The first section of Table 2 gives the magnetic properties of the MBFs. The rms values are evaluated over selected spatial pixels of the full time sequence of the models. The first row is the rms of the vertical component of the magnetic field in the area where $|B_z(z_0)| > 1000$ G (the magnetic mask) at the height where the horizontal (over the full area) and temporal mean Rosseland optical depth $\tau_R = 1$, i.e., at $z_0 = \langle\langle z(\tau_R = 1)\rangle\rangle_t$. This component is moderately decreasing with increasing effective temperature because the surrounding mean gas pressure, p_{gas}, listed in row 8 of Table 2, decreases as well. For a given optical depth, the column mass density of cooler models is higher than that of warmer models, which is simply due to the increase in opacity with increasing temperature in the present range of temperatures and gas pressures, hence the decrease in gas pressure with increasing temperature at a given optical depth. Since the surrounding gas pressure must mechanically balance the pressure exerted by the magnetic field, $p_{mag} = B^2/(8\pi)$, its strength must decrease with decreasing external gas pressure. But the change from K8V to F5V, i.e., from 1438 G to 1248 G, is a decrease of only 24.7% in magnetic pressure, while the gas pressure decreases by 72%. In fact, the rms of the magnetic field strength on the surface $\tau_R = 1$ proper and for the mask with $|B_z(\tau_R = 1)| > 1000$ G, given in row 2 of Table 2, shows no clear tendency with spectral type and can be considered constant at approximately 1560 G. We note that values in the second section of Table 2 are also averages over space and time, but p_{gas}, p_{dyn}, and p_{tot} are averages over the area outside of the magnetic mask at $z = z_0$, i.e., where $|B_z(z_0)| < 1000$ G, while p_{mag} is the average over the area of the magnetic mask.

Instead of comparing with the gas pressure, we can, more intuitively, compare with the thermal equipartition field strength $B_{eq\,th} = \sqrt{8\pi\langle p_{gas}\rangle}$, which is the field strength that exerts as much (magnetic) pressure as gas pressure $\langle p_{gas}\rangle$. This quantity is given in row 12 of Table 2. Comparing row 12 with row 1 we readily find that the strength of the magnetic flux concentrations, by far, do not reach thermal equipartition for the K-type atmospheres, but reach close to equipartition for the model F5V. In fact, maximal field strengths can reach super-equipartition for models G2V and F5V as already noted by Steiner et al. (2014). This is now confirmed in the present work, which shows $\max(|B_z(z_0)|)$ in row 3. The mean over all spectral types of the maximal field strength at $\tau_R = 1$ proper is 2848 G. Within the given standard deviations, $\max(B_z(\tau_R = 1))$ can be said to be independent of spectral type from K8V to F5V, which is an important and unexpected result first found by Steiner et al. (2013); Steiner et al. (2014) and subsequently confirmed and extended to a wider range of

spectral types and various initial magnetic field strengths by Beeck et al. (2015a).

Comparing the field strength of the magnetic elements with $B_{\mathrm{eq\,th}}$, we make implicitly use of magnetohydrostatics and the zeroth order thin flux-tube approximation. In this case, $\max(B(z))$ cannot surpass $B_{\mathrm{eq\,th}}$, but this is obviously the case here for models G2V and F5V. However, in hydrodynamics, we should add the dynamic pressure $p_{\mathrm{dyn}} = \rho v^2/2$ to the gas pressure to obtain the total pressure

$$p_{\mathrm{tot}}(z_0) = \left\langle \left\langle p_{\mathrm{gas}} + \frac{\rho v^2}{2} \right\rangle_{z_0} \right\rangle_t , \tag{4}$$

where ρ is the mass density and v the absolute velocity, which is assumed to be due to turbulent motion on relatively small scales outside of the magnetic flux concentration. Correspondingly, we can define a total equipartition field strength

$$B_{\mathrm{eq\ tot}}(z_0) = \sqrt{8\pi p_{\mathrm{tot}}(z_0)}, \tag{5}$$

which is listed in row 14 of Table 2. Now, we see that $\max(|B_z(z_0)|)$ (row 3) is smaller than $B_{\mathrm{eq\ tot}}(z_0)$ (row 14) for all models but F5V. Clearly, the dynamical pressure is important in providing the pressure balance for the strongest magnetic flux concentrations in the Sun and warmer atmospheres. The remaining force to balance super-equipartition in model F5V comes probably from magnetic tension forces that allow for larger field strength in the central part of the flux concentration than in its periphery, even for relatively thin flux tubes (Steiner et al. 1986). In case of the cooler models, the maximum field strength at z_0 is significantly below $B_{\mathrm{eq\,th}}$, which indicates that their formation and evacuation is less efficient than in warmer atmospheres (Rajaguru et al. 2002). This issue is further discussed in Sect. 6.

Figure 4 shows histograms of the magnetic field strength at the height $z = z_0$ in the top two panels and on the surface $\tau_{\mathrm{R}} = 1$ in the bottom two panels. The panels on the left-hand side show the areal fraction occupied with magnetic fields of a certain range in strength, which is equivalent to the probability of finding a certain field strength range in a given area. The panels on the right-hand side give the fraction of the unsigned magnetic flux occupied with magnetic fields of a certain range in strength. Also shown for all these probability densities is the corresponding cumulative distribution function (cdf), i.e., the probability distribution. The cdf is the running integral of the probability density; this function gives the fraction of the area (left panels) or the fraction of the total unsigned magnetic flux (right panels) that harbors a field strength above or below a certain threshold (see Steiner 2003, for intuitive examples).

For example, from the top right panel we can now read that at $z = z_0$ magnetic fields of strengths less than 500 G contribute to only ≈40% of the total absolute magnetic flux, or, fields of less than 50 G to only ≈12%; fields stronger than these limits, respectively, make up for the rest of the flux. On the other hand, the top left panel tells us that 96% of the total area harbors magnetic fields of strengths less than 500 G, or 84% less than 50 G and only the remaining 4% has fields that surpass the limit of 500 G. We note that in terms of magnetic energy, the weak fields are even less significant than they are in terms of magnetic flux because of $E_{\mathrm{mag}} \propto B^2$.

All the histograms of Fig. 4 show two maxima. A first maximum in the area fractional distribution at z_0 is at low magnetic field strengths of $B_{z\,\mathrm{weak}} \approx 5{-}20$ G, which is due to the large area of mostly granular interiors virtually void of magnetic fields. A second maximum is of strong magnetic field of 1–2 kG, which is due to the magnetic flux concentrations of the MBFs. The field strength of this second peak is given in rows 5 and 6 of Table 2 and was determined by a Gaussian fit to this peak of the area fractional distributions (panels on the left-hand side). Like the rms-values of the magnetic field strength at both heights (rows 1 and 2), also $B_{z\,\mathrm{strong}}$ hardly depends on the spectral class and is consistent with a constant value within the standard deviations. However, the precise value is sensitive on the bin size of the histogram.

The panels on the left-hand side of Fig. 4 show high frequency at low field strength and low frequency at high field strength, which is expression of the fact that only a small area is covered with strong fields, i.e., the filigree. The panels on the right-hand side on the contrary have a high peak at strong fields and a low peak at low field strengths, which tells us that most magnetic flux occurs in concentrated form of a strength in the kG range. There are differences between spectral types. While model K2V has 57% of the total absolute magnetic flux at $z = z_0$ with a field strength of 1 kG or stronger (dotted curves in the top right panel of Fig. 4), the solar model has only 43% of its total flux surpassing 1 kG. It seems that the solar model gathers magnetic flux less efficiently into MBFs than all other models, of which the most efficient is K2V. This exceptional behavior of the Sun is probably due to the 12.9% lower surface gravity of the solar model compared to all other models (see Table 1).

Row 7 of Table 2 gives the rms of B_z over the full horizontal section A at $z = z_0$. It is again virtually independent of spectral type. Beeck et al. (2015a) have demonstrated that its value can be estimated with the help of a two component model having a strong magnetic field, B_{strong}, occupying the area fraction fA and a weak component $B_{\mathrm{weak}} \approx 0$ in the rest of the area. We note that the total magnetic flux at the start of the simulation is $B_0 A$ and that the field remains largely unipolar with the present simulation setup. We then obtain for this two component model an rms of $\langle B^2\rangle^{1/2} = (B_0 B_{\mathrm{strong}})^{1/2}$. Keeping B_{weak} non-zero, we obtain

$$\mathrm{rms}(B_z) = \sqrt{B_{\mathrm{weak}}^2 + f(B_{\mathrm{strong}}^2 - B_{\mathrm{weak}}^2)}, \tag{6}$$

and for the filling factor

$$f = \frac{B_0 - B_{\mathrm{weak}}}{B_{\mathrm{strong}} - B_{\mathrm{weak}}} = \frac{\mathrm{rms}(B_z)^2 - B_{\mathrm{weak}}^2}{B_{\mathrm{strong}}^2 - B_{\mathrm{weak}}^2}. \tag{7}$$

In the present case, we have $B_0 = 50$ G, $B_{\mathrm{strong}} \approx 1491$ G (mean of $B_{z\,\mathrm{strong}}(z_0)$ over all models), and $B_{\mathrm{weak}} \approx 10$ G (see Fig. 4, top left panel), which gives according to Eq. (6) $\mathrm{rms}(B_z) = 245$ G in excellent agreement with the actual values in row 7. For the filling factor results from Eq. (7) $f = 0.027$, which is in acceptable agreement with the values given in row 32 of Table 2.

5. Radiative properties

The third and fourth sections of Table 2 present the results concerning the radiative intensity and radiative flux for each simulated spectral type of stellar atmospheres and the effect of small-scale magnetic fields on these quantities.

5.1. Effective temperature and intensity contrasts

First, we look at the actual effective temperature, T_{eff}, of each model. The effective temperature is listed in row 17 of Table 2 and is computed with the help of the Stefan–Boltzmann law,

$$T_{\mathrm{eff}} = \sqrt[4]{\langle F_{\mathrm{bol}}\rangle_t/\sigma}, \tag{8}$$

where σ is the Stefan–Boltzmann constant and $\langle F_{\rm bol}\rangle_t$ the time-averaged, bolometric radiative flux that leaves the computational domain across its upper boundary. The actual effective temperature, $T_{\rm eff}$, differs from the corresponding nominal value, $T^*_{\rm eff}$, given in Table 1, by less than about 1%. Taking the instant radiative flux, $F_{\rm bol}(t)$, we can plot the effective temperature as a function of time, which is done in Fig. 5. Apart from an initial, approximately 2000 s lasting transient phase (which is due to the regridding and to the insertion of the magnetic field as explained in Sect. 2.2), the effective temperature stays fairly constant with time but fluctuates; increasingly with increasing effective temperature up to G2V. The standard deviation of this fluctuation is also given in row 17 of Table 2. The origin of the fluctuation is the dynamic nature of the models, which produces bright granules and dark intergranular lanes of different size and brightness as a function of time and the gas-pressure driven (p-mode) oscillation in the model. Thus, the larger the model (in terms of spatial scales) the smaller the fluctuation is expected to be (because of averaging effects) such that fluctuations of a global main-sequence atmosphere with $\log g = 4.5$ are expected to be orders of magnitude smaller (see, e.g., Ludwig 2006; Bastien et al. 2013; Ludwig & Steffen 2016) than what the present small boxes produce.

From row 17 of Table 2, one may guess that the models with magnetic field have a systematically higher effective temperature, and therefore higher radiative flux, than the non-magnetic models, but the difference is within the standard deviation of the fluctuations. In Sect. 5.2 we use a cumulative mean for judging the significance of the mean values, but first we have again a look at contrast values. In Sect. 3.1, we discussed the rms granular contrast in bolometric, vertically directed intensity, given in row 21 of Table 2, and found no systematic difference between the magnetic and non-magnetic models. Restricting the evaluation of the intensity fluctuations to the magnetic filigree, we compute

$$c_{\rm MBF\,rms} = \left\langle \frac{\sqrt{\langle (I_{\rm bol} - \langle I_{\rm bol}\rangle)^2\rangle_{\rm MBF}}}{\langle I_{\rm bol}\rangle} \right\rangle_t , \tag{9}$$

where $\langle\cdots\rangle_{\rm MBF}$ is the average over all areas with $B_z(z_0) > 1$ kG and $\langle I_{\rm bol}\rangle$ is still the mean bolometric intensity of the magnetic model. It has a maximum at spectral type K2V (see row 22 of Table 2) and is significantly larger than $c_{\rm rms}$, except as of F5V for which the MBFs are significantly less bright than the granules. The latter statement can be quantified by computing the contrast between the magnetic filigree and granules as

$$c_{\rm MBF-gran} = \left\langle \frac{\langle I_{\rm bol}\rangle_{\rm MBF} - \langle I_{\rm bol}\rangle_{\rm gran}}{\langle I_{\rm bol}\rangle_{\rm gran}} \right\rangle_t , \tag{10}$$

where $\langle I_{\rm bol}\rangle_{\rm gran}$ is the spatially averaged intensity, over all granules, with granules defined as explained in Sect. 2.2. This contrast value is given in row 24 of Table 2 from which we can see that only model K2V has a filigree that is significantly brighter than the granules, while for model F5V it is significantly darker. However, we note that the filigree is still much brighter than the intergranular space in any case. The intergranular space is partially replaced by the filigree such that the magnetic models can be expected to be, over all, brighter than the non-magnetic models.

The maximum contrast of MBF is given by

$$c_{\rm MBF\,max} = \left\langle \frac{\max(I_{\rm bol\,MBF}) - \langle I_{\rm bol}\rangle}{\langle I_{\rm bol}\rangle} \right\rangle_t , \tag{11}$$

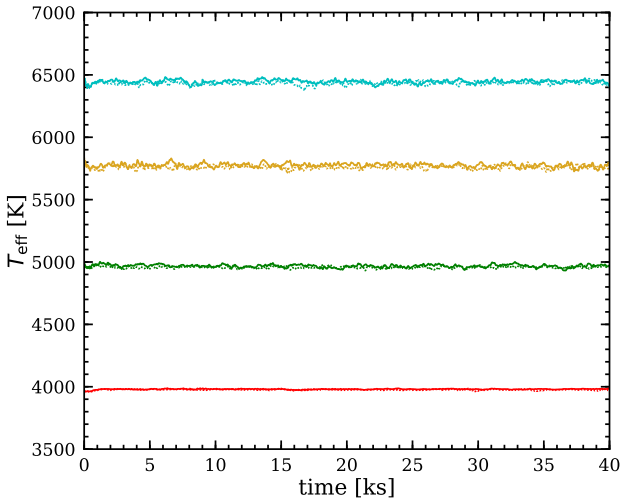

Fig. 5. Effective temperature as a function of time of the non-magnetic models (dotted curves) and of the magnetic models (solid curves) for all four spectral types F5V to K8V from *top* to *bottom*, respectively.

where again, $I_{\rm bol\,MBF}$ is the intensity within the area where $B_z(z_0) > 1$ kG. The values are given in row 23 of Table 2 and vary between 49 and 86%. Especially the spectral type K2V shows a large maximum; it also exhibits the largest difference $c_{\rm MBF\,rms} - c_{\rm rms}$ and is the only model whose filigree is significantly brighter than the granules. For the solar model G2V, this value is 72%, which renders the brightest magnetic elements a conspicuous feature even in maps of the continuum intensity.

For a qualitative comparison, the mean continuum contrasts of solar magnetic bright points were measured with the 1 m Swedish Solar Telescope SST to be 10–15% at 588 nm (Wiehr et al. 2004) and with the 1 m Sunrise balloon-borne solar telescope to be 11% at 525 nm (Riethmüller et al. 2010). These values are lower but qualitatively comparable to the bolometric contrast of $c_{\rm MBF\,rms} = 18.7\%$ that we obtain for the solar model. This, however, has a spatial resolution that is rather comparable to a 3 m class telescope, unlike the 1 m of the observations.

5.2. Radiative surplus of the magnetic models

Figure 6 shows for the solar model (G2V) the bolometric intensity of the vertically propagating radiation (*left*) and the bolometric radiative flux (*right*) that leaves the computational domain through the top boundary as a function of time for both the magnetic (blue curve) and non-magnetic model (red curve). Here, the radiative flux is given by

$$F_{\rm bol}(t) = \left\langle \int_{4\pi} I_{\rm bol}(\boldsymbol{n}, t)\, \boldsymbol{n}\cdot\hat{\boldsymbol{z}}\, {\rm d}\Omega \right\rangle , \tag{12}$$

where $\boldsymbol{n}$ is the unit vector in propagation direction of the radiative intensity $I_{\rm bol}(\boldsymbol{n}, t)$, $\hat{\boldsymbol{z}}$ is the unit vector pointing upward in the vertical direction (normal to the top boundary), and $I_{\rm bol}(\boldsymbol{n}, t)$ is evaluated at the top boundary. The integral is taken over all solid angles and the average is taken over the top boundary. Correspondingly, the radiative intensity in the left panel of Fig. 6 is given by

$$I_{\rm bol}(t) = \langle I_{\rm bol}(\hat{\boldsymbol{z}}, t)\rangle . \tag{13}$$

In Fig. 6 and following figures, $I_{\rm bol}(t)$ and $F_{\rm bol}(t)$ are normalized to the respective time averaged intensity $\langle I_{\rm bol\,0}\rangle_t$ and

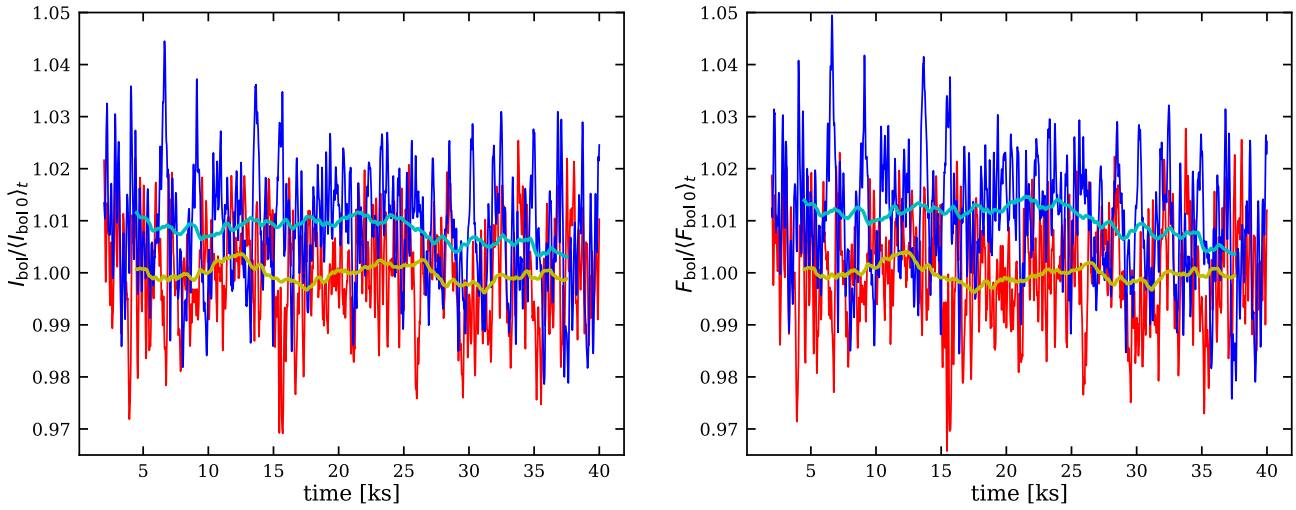

Fig. 6. Bolometric radiative intensity (*left*) and bolometric radiative flux (*right*) leaving the computational domain in the vertical direction through the top boundary as a function of time for both the magnetic (blue curve) and non-magnetic (red curve) solar model (G2V). The cyan and orange curves are the moving (box car) average of the magnetic and non-magnetic models, respectively, using a time window-width of 5000 s.

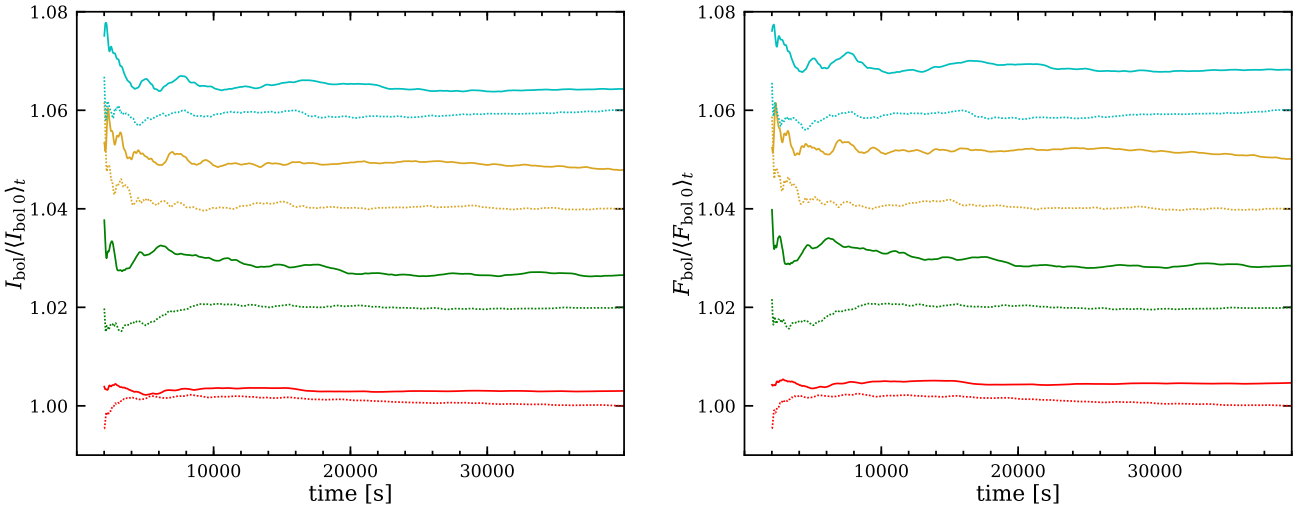

Fig. 7. Cumulative means according to Eq. (14). *Left*: cumulative mean of the bolometric radiative intensity, Eq. (13). *Right*: cumulative mean of the bolometric radiative flux, Eq. (12). The solid curves refer to the magnetic models and the dotted curves to the magnetic field-free models. For better visibility, successive pairs of curves are shifted by 0.02 in ordinate direction and the lowermost (red) curves are unshifted and refer to spectral type K8V. The subsequent, shifted curves refer (from *bottom* to *top*) to spectral types K2V (green), G2V (gold), and F5V (blue).

flux $\langle F_{\rm bol\,0}\rangle_t$ of the non-magnetic model. $\langle I_{\rm bol\,0}\rangle_t$ and flux $\langle F_{\rm bol\,0}\rangle_t$ are given in, respectively, rows 18 and 19 of Table 2 for reference, where we omitted the brackets for simplicity. Plots, such as those of Fig. 6 for spectral types other than the Sun, look similar and are compiled in Appendix A. Despite the fluctuations, we see a clear difference between the non-magnetic and magnetic model, the latter having higher intensities and fluxes.

For the solar model of Fig. 6, the difference of the temporal mean is 0.79% in intensity and 1.02% in radiative flux. The standard deviation of the fluctuations in these differences is ±1.5%. From the running means in Fig. 6 and Appendix A, we see that there are also long-term trends present in $I_{\rm bol}(t)$ and $F_{\rm bol}(t)$, and notably there is a decline toward the end of the magnetic solar model, a global decline of the non-magnetic model K8V, an increase in the second half of the non-magnetic model F5V, and a decline at the beginning of the magnetic K2V model. The origin of these trends is unknown but they are less significant than the differences in intensity and flux between the non-magnetic and magnetic models. Finally, the intensity and flux of the magnetic models tend to fluctuate slightly more than those of the corresponding non-magnetic models except for model K8V. This is probably due to the appearance and vanishing of MBFs in the magnetic model.

The trends and differences become more apparent than in Figs. 6 and A.1, when plotting the cumulative mean, which is done in Fig. 7. It is given by

$$\langle f\rangle\,(N;N_{\rm start}) = \frac{1}{N-N_{\rm start}+1}\sum_{i=N_{\rm start}}^{N} f_i, \quad N > N_{\rm start}, \tag{14}$$

where $N_{\rm start}$ indicates the index of the start time of the time-series analysis, i.e., in our case $t_{N_{\rm start}} = 2000$ s, N the index of the time up to which the mean is taken, and f_i is the quantity of the time series, i.e., the vertical bolometric intensity, or radiative flux. We recall that f_i has a cadence of 10 s. From this plot, we see that the time series are long enough to compute accurate mean values because fluctuations after $t \approx 20\,000$ s are much smaller

than the differences between the non-magnetic (doted curve) and magnetic models (solid curves).

These differences are given in rows 25 and 26 of Table 2, which are the mean differences in intensity and flux between the magnetic and non-magnetic models in the time period from 2000 s to 40 000 s. In terms of cumulative means, these differences between the magnetic and non-magnetic models are formally given as

$$\delta_{I_{\rm bol}}(N) = \frac{I_{\rm bol\,mag}(N;N_{\rm start}) - I_{\rm bol\,0}(N;N_{\rm start})}{I_{\rm bol\,0}(N;N_{\rm start})}, \quad (15)$$

$$\delta_{F_{\rm bol}}(N) = \frac{F_{\rm bol\,mag}(N;N_{\rm start}) - F_{\rm bol\,0}(N;N_{\rm start})}{F_{\rm bol\,0}(N;N_{\rm start})}, \quad (16)$$

where $I_{\rm bol\,mag}$ and $F_{\rm bol\,mag}$ refer to the magnetic and $I_{\rm bol\,0}$ and $F_{\rm bol\,0}$ to the non-magnetic model and $t_N = 40\,000$ s.

There are two standard deviations given in rows 25 and 26. The first is the standard deviation in the fluctuation of the difference $I_{\rm bol\,mag}(t) - I_{\rm bol\,0}(t)$ and $F_{\rm bol\,mag}(t) - F_{\rm bol\,0}(t)$, respectively, in the time period from 2000 s to 40 000 s. The second set is the standard deviation in the fluctuation of the difference of the cumulative mean, i.e., $\delta_{I_{\rm bol}}(N)$ and $\delta_{F_{\rm bol}}(N)$ in the time period for 20 000–40 000 s. This latter σ is a measure for the stability of the mean difference. It is approximately ten times smaller than the mean intensity and flux differences between magnetic and non-magnetic models, indicating that these mean differences stay very stable in time.

From rows 25 and 26 of Table 2 and Fig. 7 we see that $\delta_{I_{\rm bol}}$ and $\delta_{F_{\rm bol}}$ are always positive, meaning that the magnetic models have always a larger mean intensity and a larger radiative flux than the non-magnetic models, where the solar model (G2V) has the largest surplus in intensity and flux. Also we see that the surplus in radiative flux always exceeds that of the intensity. This finding is further explored in Sect. 6.

6. Wilson depression, hot wall effect, and convective collapse

In this section, we more deeply explore the physics of MBFs. In particular, we investigate the surface depression at the location of MBFs, the effect that this depression has on the radiative intensity and flux, and on the formation process of MBFs, all as functions of spectral type of the stellar atmospheres under consideration.

6.1. Wilson depression

Within a photospheric magnetic flux concentration, the atmosphere is rarified with respect to the surroundings. This follows from lateral mechanical equilibrium, by which the surrounding gas and dynamical pressure must balance the magnetic pressure plus internal gas pressure of the flux concentration. Since in photospheric layers lateral thermal equilibrium is efficiently established by radiation, the temperature does not vary much in the horizontal direction and therefore the density must be low for a correspondingly low internal gas pressure. Because of the rarified flux-tube atmosphere, its optical depth scale is shifted downward with respect to the scale in the surrounding atmosphere. In particular, there is a difference in the average height of the surface of optical depth unity inside the magnetic flux concentration relative to the surrounding atmosphere (where this height is at $z0$). We call this difference WD, in reminiscence of the Wilson depression of sunspots and speak of a depression of

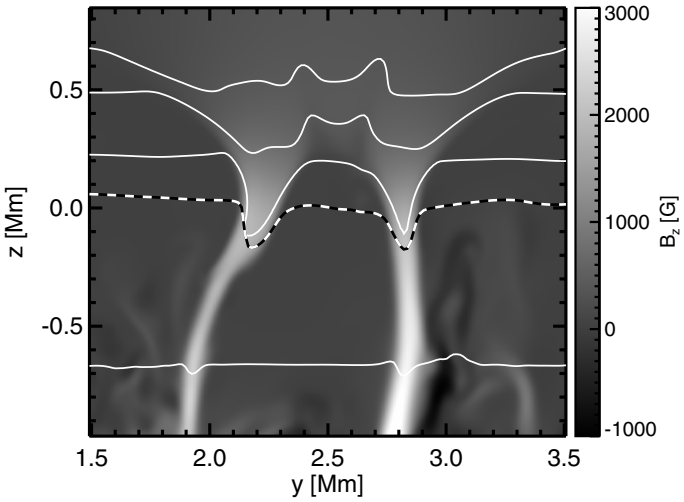

Fig. 8. Vertical section through the magnetic solar model (G2V) at time $t = 16\,552$ s, showing in gray scales the vertical magnetic field strength. Two neighboring magnetic flux concentrations exhibit each a distinct WD in the $\tau_{\rm R} = 1$ contour (dashed curve) of approximately 180 km depth. The solid white curves are contours of constant density of $\rho = 10^{-6}$, 10^{-7}, 10^{-8}, and 10^{-9} [g cm^{-3}] from bottom to top.

the $\tau_{\rm R} = 1$ surface at the location of the magnetic flux concentration. Two example depressions of model G2V are shown in Fig. 8. The optical depth surface $\tau_{\rm R} = 1$ is computed for vertically directed lines of sight. We note the substantial rarefaction in the surface layers of the flux concentrations that renders these layers more transparent for radiation than layers at the same geometrical height in the surrounding medium.

Histograms of the WD of MBFs of the considered stellar atmospheric models are given in Fig. 9. The histograms in the panel on the left-hand side depict the number of MBFs, for each bin of WDs, normalized by the total number of MBFs. The procedure for computing the number of MBFs is given in Appendix B. The WD of an individual MBF is in the present paper determined as the average over 5% of its area with largest depression with respect to the reference level $z0$. Since large MBFs generally have a deeper depression, the corresponding area weighted histograms are also shown on the right-hand side of Fig. 9. The corresponding temporal mean values are given in rows 28–31 of Table 2.

The WD strongly increases with increasing effective temperature in accordance with expectations because of the increase in pressure scale height, $H_{\rm p}$. The latter quantity is listed in Table 1. However, as was already noted in the preliminary study of Steiner et al. (2014), the WD increases more rapidly than the pressure scale height. While its mean value is 0.5–$0.7 \times H_{\rm p}$ in the case of the K8V model, it is 1.6–$2.7 \times H_{\rm p}$ in the case of the F5V model and 1.1–$1.6 \times H_{\rm p}$ for the solar model. If WD was strictly proportional to $H_{\rm p}$, then $B_z(z_0)$ would be proportional to $B_z(\tau_R = 1)$ because $B_z(z) \propto B_z(\tau_R = 1)\,{\rm e}^{-z/(2H_{\rm p})}$ according to the zeroth order thin flux-tube approximation. Since $B_z(\tau_R = 1)$ is approximately constant with effective temperature, so would $B_z(z_0)$. But since WD grows stronger than $H_{\rm p}$, $B_z(z_0)$ must decrease with effective temperature, which is what we observe in our simulations as stated in Sect. 4 and quantified in rows 1 and 3 of Table 2.

6.2. Hot wall effect

The WD enlarges the effective surface from which the radiation can escape with the consequence of a locally enhanced radiation

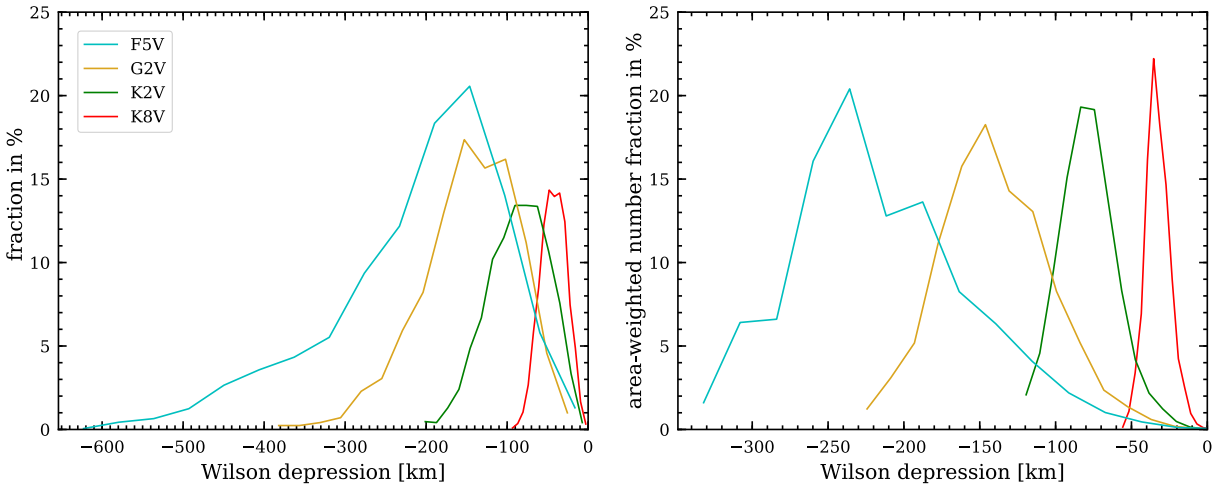

Fig. 9. Histograms of the WD (*left*) and the same histograms, but weighted by the size (area) of the MBFs (*right*). The bin size is variable from 4.8 km for K8V to 24.3 km for F5V to keep a constant bin number of 15 for each spectral type. Colors indicate various spectral types according to the inserted legend on the *left panel*. The histograms are based on the geometric maps of the $\tau = 1$ surface of the full time series.

field acting as a heat leak at the solar surface. In particular, radiation can escape from the walls of the depression: preferentially in directions inclined from the vertical (i.e., more perpendicular to the walls). Since the magnetic flux concentrations rapidly expand with height, the hot walls do so as well, which makes them clearly visible also for vertical lines of sight, but also because the flux concentrations are often inclined with respect to the vertical direction. This is known as the hot wall effect of magnetic flux concentrations and is responsible for these concentrations to appear bright in the form of MBFs. The cooling caused by the wall radiation is efficiently compensated for by convective energy transfer toward the walls in the surroundings of the field concentration (Spruit 1976). However, it is not only the walls of the depression proper that enhance the radiative flux. At least as important is the partial evacuation of the magnetic flux concentration, which leads to a rarified, optically more transparent flux-tube atmosphere across which radiation from a larger surrounding of the field concentration proper can escape more easily (Steiner 2005). This effect causes granules limbward of magnetic flux concentrations, when observed near the limb, to appear bright as facular granules. Again in this case, the enhanced radiation propagates in directions inclined from the vertical.

According to Eq. (12), the vertically directed radiative flux takes intensities propagating in all directions into account, while $I_{\rm bol}$, according to Eq. (13), is the intensity propagating in the vertical direction alone and is therefore enhanced only in an area, which is the projection of the hot walls onto the horizontal plane. Since the hot wall effect and the effect of the rarified atmosphere causes enhanced radiation in preferentially inclined directions, we expect MBFs to affect $F_{\rm bol}$ more than $I_{\rm bol}$. This is in fact the case as we can see from rows 25 and 26, where $\delta_{F_{\rm bol}}$ is always larger than $\delta_{I_{\rm bol}}$ for all spectral types. Moreover, since the WD and the degree of evacuation strongly increases with effective temperature, the difference $\delta_{F_{\rm bol}} - \delta_{I_{\rm bol}}$ (given in row 27 of Table 2) increases toward the hotter end of the spectral sequence. In other words, cool stellar atmospheres have WDs that are small in comparison to the horizontal extent of their MBFs and their magnetic field concentrations are not much rarefied, which renders the hot wall effect weak and facular granules feeble. Correspondingly, the difference in radiative intensity and flux between magnetic and non-magnetic models is small. Vice versa, in the solar and warmer atmospheres, the WD is substantial and the degree of evacuation high, which renders the hot wall effective and facular granules bright and therefore the difference in radiative intensity and flux between magnetic and non-magnetic models is large and also the difference between the radiative intensity and flux surpluses of the magnetic model is significantly larger than in case of the K-type atmospheres.

6.3. Convective collapse

When starting the simulations of the magnetic models with a homogeneous vertical magnetic field of 50 G, MBFs form within a few minutes. Subsequent to this formation process and magnetic field intensification, the MBFs are shuffled around, get deformed, merge, and break apart to form larger and smaller MBFs, or, less often, dissolve again. Only a minor fraction of the magnetic flux remains in the form of a weak field component (see Fig. 4) that is available to form MBFs anew. The initial magnetic intensification is probably best described by the concept of the convective collapse (Parker 1978; Webb & Roberts 1978; Spruit 1979; Spruit & Zweibel 1979), although caution is indicated, since the real process is more involved than this highly idealistic, quasi-static process suggests.

If the formation process was highly efficient, then the magnetic flux concentration would be evacuated and the field strength would reach thermal or thermal plus dynamic equipartition. In Sect. 4, we found that in reality only peak field strengths approach equipartition for the solar atmosphere and even surpass it for model F5V but that the formation process is not fully efficient and the field strength at $z = z_0$ stays far below the equipartition values for the K-type atmospheres. Thus, the convective intensification seems to be moderately efficient for cool stellar models but highly efficient for the Sun and warmer stars.

One important ingredient in the convective collapse theory is the superadiabaticity in the top layers of the convection zone. In fact, the convective collapse lives on this potential, which is the difference between the real and the adiabatic temperature gradient, $\delta = \nabla - \nabla_{\rm ad}$, where $\nabla = {\rm d}\ln T/{\rm d}\ln p$ and likewise $\nabla_{\rm ad}$ for the adiabatic displacement of a plasma parcel. Hence, we can expect the magnetic field intensification to be the more efficient

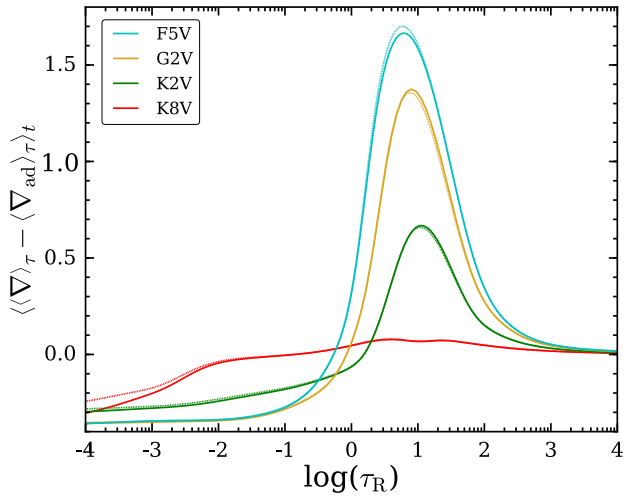

Fig. 10. Superadiabaticity $\delta = \nabla - \nabla_{\rm ad}$ as a function of optical depth for spectral types K8V to F5V, color coded according to the legend. Solid curves refer to the magnetic models, and dotted curves to the non-magnetic models.

the larger the superadiabaticity δ (Rajaguru et al. 2002). This is indeed the case as can be seen from Fig. 10, which shows the superadiabaticity δ as a function of optical depth for all models. Clearly, the superadiabaticity in the subsurface layers is well developed for the models F5V and G2V, is less strong and shifted further down into the convection zone for K2V, and is poorly developed in K8V. Correspondingly, the intensification is less efficient in model K8V and the flux concentrations are far from being evacuated as can be seen from the density ratio and the plasma β given in rows 15 and 16 of Table 2. There, $\rho_{\rm int}/\rho_{\rm ext}(z_0)$ is the fraction of the mean density at the height z_0 that remains in the rarefied atmosphere of MBFs and β is the ratio of gas pressure to magnetic pressure within MBFs at the same height, z_0. Both quantities tell us that the degree of evacuation of MBFs monotonically increases with increasing effective temperature, which is a consequence of the monotonic increase of the superadiabaticity in the surface layers with increasing $T_{\rm eff}$.

For completeness we note that four decades of optical depth below the surface of $\tau_{\rm R} = 1$, the superadiabaticity drops below 2×10^{-2} but continues to stay positive with depth in all models. The subadiabaticity starts at $\tau \approx 0.5$ for the model F5V but already at $\tau \approx 1.5$ for model K2V such that the convectively stable layers reaches the deeper (in terms of optical depth) the cooler the spectral type. In between these limits, the superadiabaticity assumes a peak value, which shifts to optically deeper levels when going from warmer to cooler models, hence the veiled granules of cool spectral types. K8V is an exception in that its superadiabaticity remains low but positive (with a peak value of 0.08) all the way from the deep layers up to $\tau \approx 0.1$.

Similar runs for $\delta(\tau)$ from non-magnetic simulations of diverse spectral types using different simulation codes have been obtained by Beeck et al. (2013a, Fig. 11, right panel) and by Magic et al. (2013a, Fig. 25).

7. Discussion

In the following, we assess some of the results obtained in the previous sections in terms of observations and results from previous work and we review the assumption of the constant deep adiabat.

7.1. Radiative surplus due to MBFs

A principal result of this paper is that the magnetic models unanimously show a surplus in radiative intensity and radiative flux with respect to their corresponding non-magnetic model for all stellar types and for the unique initial magnetic flux that we considered. The surplus is maximal for the solar model, but depending on the time span taken for the average, the K2V model has similarly large surpluses. For all models, the surplus in radiative flux is larger than that of the vertically directed radiative intensity alone. The surplus of radiative flux of the solar magnetic model on the order of 1% may appear large in comparison to the peak-to-peak variation of the total solar irradiance (TSI) over the solar cycle of ≈1 ‰ (Fröhlich 2013). However, rather than take the combined effects of spots and small-scale magnetism into account, we took the latter alone and we computed the extremal difference between a model that represents magnetic network or plage regions and a model completely void of magnetic fields. On the real Sun, large areas of the solar disk may be more quiet than our solar model, even at times of solar maximum. On the other hand, there is no region completely void of magnetic fields. Also, the relative variation of TSI may go up to 0.2% on short timescales of several days. In case of the Sun, sunspots reduce the TSI and therefore counterbalance the effect from the small-scale magnetism, which, taken alone, would be much larger than 1 ‰.

The surpluses of the vertically directed bolometric intensities obtained in Sect. 5.2 are in good agreement with those preliminarily found by Steiner et al. (2014) for the same spectral types as considered here but with much shorter time series and an approximative, less expensive method for the determination of the surpluses. Steiner et al. (2014) had values of $\delta_{I_{\rm bol}} = 0.32, 0.79, 0.62$, and 0.46% for the spectral types K8V, K2V, G2V, and F5V[1], respectively, compared to 0.30, 0.65, 0.79, and 0.43% of row 25 of Table 2 of the present work. As in Steiner et al. (2014), we find again the smallest surplus for the coolest model (K8V) and a decline from G2V to F5V.

The agreement with the results of Beeck et al. (2015b) is good as well. These authors also obtained surpluses in the vertically directed bolometric intensities of the magnetic over the non-magnetic run. From Table 1 of Beeck et al. (2015b), we derived for their models with 100 G initial field strength $\delta_{I_{\rm bol}} = 0.20, 0.31, 1.08, 1.38, 1.50$, and 0.10% for the stellar types M2V, M0V, K5V, K0V, G2V, and F3V, respectively. Again, the surplus is maximal for the solar model and steeply drops toward the warmer model (F3V) and the coolest models (M2V and M0V).

The radiative surpluses of the magnetic over the non-magnetic models obtained here and previously by Steiner et al. (2014) and Beeck et al. (2015b) are in sharp disagreement with the results of Thaler & Spruit (2014) who found a radiative deficit of −0.34% for a solar magnetic simulation with a mean flux density of 50 G. At present, we do not know the origin of this disagreement. To find out if it is a real difference in the simulation or if it is due to different analytical methods, we plan, as a first step, to apply the analytical procedure of Thaler & Spruit (2014) to our present solar model.

7.2. Entropy of the deep adiabat

The underlying fundamental assumption of the present comparison between model atmospheres with and without magnetic field is that the specific entropy of the material entering the computational domain from below across the bottom boundary is

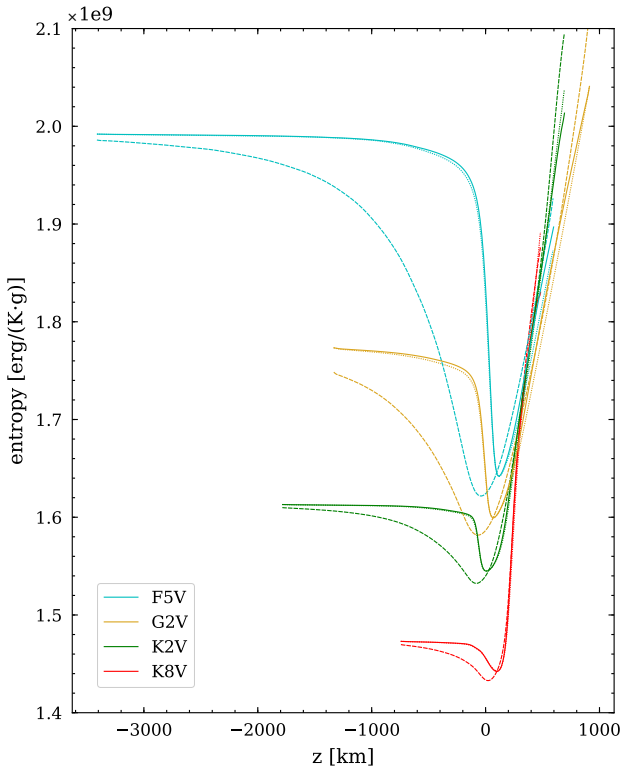

Fig. 11. Specific entropy of the upflowing plasma of the magnetic (solid curves) and the non-magnetic (dotted curves) atmospheres as a function of geometrical height z. Colors refer to the various spectral types according to the inserted color legend. The dashed curves show the specific entropy in the downdrafts of the non-magnetic models.

identical in both cases. This means that we assume this entropy to be unaffected by the presence or absence of surface magnetic fields. Since the boundary conditions are kept the same for both magnetic and non-magnetic simulations, the specific entropy of the entring plasma, $s_{\rm inflow}$, is the same, in agreement with our fundamental assumption. Any change of $s_{\rm inflow}$ would change $T_{\rm eff}$, which in turn would change the determination of $\delta_{I_{\rm bol}}$ and $\delta_{F_{\rm bol}}$.

But the question remains whether this fundamental assumption is justified. The ascending plasma is assumed to have the entropy of the adiabat of the deep convective envelope (Ludwig et al. 1999). This adiabat is independent of the magnetic field only if (i) the convective downdrafts mix and thermalize to the same degree with the ascending flow in both the magnetic and the non-magnetic simulations, or (ii) there is no mixing of the continuously ascending plasma with the descending plasma, or (iii) this mixing and thermalization are unimportant. With regard to the last point (iii), in fact, the heat capacity of the convection zone is huge (Spruit 1977), such that the deep adiabat indeed cannot be significantly affected by any potential extra entropy deficient downflows caused by the small-scale magnetism, at least not in the deep convection zone.

Furthermore, also (ii) is to a high degree fulfilled for the deepest layers of our models. Figure 11 shows that in all but the solar model, the mixing of plasma in the upflows with downflowing, entropy deficient plasma, must be weak because the entropy of the upflowing plasma in the layers adjacent to the bottom boundary remains essentially constant (solid curves in Fig. 11). The constancy of the deep adiabat is not reached only in the case of the solar model because the model is too shallow and therefore substantial entropy transfer from the ascending plasma to the entropy deficient downflows prevails down to the bottom boundary.

Condition (i) is to a great deal satisfied as well because the difference of the specific entropy as a function of height between the magnetic and non-magnetic simulations is very small from $z = 0$ down to the bottom boundary (difference between solid and dotted curves in Fig. 11). Even for the solar model this difference remains small proving that the degree of mixing and thermal diffusion of ascending with entropy deficient plasma is very similar in the magnetic and non-magnetic models.

The dashed curves in Fig. 11 show the entropy of the downflowing plasma. These are not constant in the convective layers but they all approach the respective deep adiabat close to the bottom boundary. This behavior shows that mixing and thermal diffusion with ascending fluid takes place in the downflows. On the other hand, little entropy exchange with downflowing fluid takes place in the upflows, proving that the assumption of a magnetic field independent deep adiabat is a good one. Caution is indicated regarding the solar model, which is too shallow. We cannot exclude the possibility that a deeper solar model would yield smaller values for $\delta_{I_{\rm bol}}$ and $\delta_{F_{\rm bol}}$, which would possibly shift the maximum in these quantities to spectral type K2V.

7.3. Wilson depression

The values for the WD listed in rows 28–31 of Table 2 and shown in the histograms of Fig. 9 are different from the values given in Steiner et al. (2014) and Beeck et al. (2015a). There are various reasons for this discrepancy. Steiner et al. (2014) gave the maximal depression of all MBF found in any of a small number of snapshots, while the present work gives the average of the maximal depression found in every individual MBF over each snapshot of the full time series. Therefore, the depressions listed in Steiner et al. (2014) are deeper than those found in the present work. In fact, the maximal occurring depressions can be found from a histogram such as that of Fig. 9, but with smaller bin size to be $\mathrm{WD_{max}} = 100, 214, 404$, and 660 km for the spectral types K8V, K2V, G2V, and F5V, respectively. These are peak values over the full time period of 10.55 h and are therefore larger in turn than the values of Steiner et al. (2014), which are 70–80% of $\mathrm{WD_{max}}$.

On the other hand, the values of Beeck et al. (2015a) tend to be smaller than those given in the present work because they represent areal averages of the depression over areas of $B(\tau_{\rm R}) > 750$ G. Here, the area is defined as $B(\tau_{\rm R}) > 1000$ G (which should increase WD by only ≈10% according to Beeck et al. 2015a) but probably more important is that the present WD is not the areal average but an average of maximal values as explained in Sect. 6.1.

7.4. Approximative determination of the radiative surplus

Steiner et al. (2014) computed the radiative surplus of the magnetic model from that model alone, without using a comparative magnetic field-free run, which is a procedure suggested by Steiner et al. (2013). Instead, these authors mimicked the comparative non-magnetic model by applying a mask to the magnetic model, which would hide the magnetic filigree from sight completely, or, alternatively, replace it with average dark intergranular lane. This method is computationally half as expensive as the procedure chosen in the present paper. As shown in Sect. 7.1 the results obtained in this way are well comparable to the results when carrying out the full non-magnetic comparative run, at least for the present range of spectral types from

K8V to F5V and for the unique initial magnetic field strength of 50 G.

This good agreement can be understood when examining Fig. 3, which reveals that for each spectral type, the histogram of the masked magnetic model and the histogram of the non-magnetic model are very similar. The difference at low intensities can be taken into account by replacing the mask with the average intensity of intergranular lanes as in Steiner et al. (2014). Hence, for the present spectral range and the purpose of intensity distributions, this finding validates the approach taken in Steiner et al. (2014).

7.5. Connection to the stellar bolometric flux

In order to relate the effect of small-scale magnetism that we found with the help of our numerical simulations to the global variations of stellar photometric fluxes, we need to relate the bolometric radiative intensity and flux as found in our simulations to this global quantity. This relationship can be straightforwardly established when assuming that the star has a quasi-homogeneous surface that is well represented by the small section that our simulation box presents. In this case, one can use the calculations of Mihalas (1978, Figs. 1–3 and corresponding text) to show that the energy flux $f_{\rm bol}$ received from the star by a distant observer is rather accurately given by

$$f_{\rm bol} \propto F_{\rm bol}, \tag{17}$$

where $F_{\rm bol}$ is the radiative flux that leaves the computational box across its top boundary as given by Eq. (12). Correspondingly, the change in the relative bolometric radiative flux of a star over a stellar cycle from a virtually field-free surface to one with a mean magnetic field strength of 50 G is equal to $\delta_{f_{\rm bol}} = \delta_{F_{\rm bol}}$ given in row 26 of Table 2. This is the contribution due to small-scale magnetism alone, which may become counter balanced by the large-scale magnetism in the form of starspots.

8. Conclusions

Simulations of the atmospheres and adjacent convective layers of four different cool main-sequence stars with effective temperatures of 4000 K (K8V), 5000 K (K2V), 5770 K (G2V, solar), and 6500 K (F5V) were performed. Each model was run in two separate settings with the only difference of starting once with an initial vertical homogeneous magnetic field with a flux density of 50 G (magnetic models), and once without a magnetic field (non-magnetic models). The two settings were intended to represent temporal phases (or spatial regions) of high and low small-scale stellar magnetic activity. Each model and setting was run for 11.1 h of which 10.5 h served for the subsequent analysis.

Basic properties of the simulation models are given in Table 1. Granular contrasts agree well with observed contrast for the solar model and with contrasts from other simulations for the stellar models. In particular, there is the steep increase of the granular contrast from the coolest to the warmest model and the proportionality of the granular size with the pressure scale height at fixed surface gravity.

All magnetic models show in bolometric intensity conspicuous, bright features that coincide with concentrations of magnetic fields, which we call magnetic bright features (MBFs), collectively also the magnetic filigree. The distributions of the bolometric intensity (intensity histograms) for the two settings show a clear difference for all model atmospheres: the magnetic models show a shoulder on the high end of the distribution that is absent in the magnetic field-free models. This is expression of the fact that the magnetic models have a slightly higher occurrence of bright pixels, which is entirely due to the magnetic filigree.

Turning to the magnetic properties of the MBFs, we find as follows: (i) at the mean height of Rosseland optical depth $\tau_{\rm R} = 1$, i.e., at $z_0 = \langle z(\tau_{\rm R} = 1)\rangle$, the magnetic field strength moderately decreases with increasing effective temperature. At optical depth $\tau_{\rm R} = 1$ proper, it stays approximately constant at around 1560 G, independent of spectral type. (ii) When comparing the field strength at z_0 with the surrounding gas pressure, we find that its energy density approaches the thermal energy density of the surrounding gas (thermal equipartition) for the warmest model F5V and is similarly high for the solar model but lower (sub-equipartition) for the models cooler than the solar model (K8V and K2V). (iii) The distribution (histogram) of the magnetic flux density at the surface $\tau_{\rm R} = 1$ is remarkably similar for all models. It has a bimodal shape with a sharp peak around 1800 G owing to the MBFs and a broad, moderate peak in the hecto-Gauss range in case of the magnetic flux fractional distribution. Most magnetic flux is concentrated, occurring as MBFs. (iv) The Wilson depression (WD) of MBFs strongly increases with increasing effective temperature – more so than the pressure scale height. While the mean WD is $0.5{-}0.7 \times H_{\rm p}$ in the case of model K8V, it is $1.6{-}2.7 \times H_{\rm p}$ in the case of the F5V model and is $1.1{-}1.6 \times H_{\rm p}$ for the solar model. Likewise, the degree of evacuation increases from $\rho_{\rm int}/\rho_{\rm ext}(z_0) = 0.75$ for model K8V to 0.36 for model F5V. (v) The superadiabaticity $\delta = \nabla - \nabla_{\rm ad}$ in the subsurface layers decreases with decreasing effective temperature from spectral type F5V to K2V and its peak value is gradually shifted to deeper layers. For model K8V, this superadiabatic peak is poorly developed. Correspondingly, the convective collapse is highly efficient for the warmer spectral types but feeble in case of K8V, which explains the low degree of evacuation of MBFs in this case.

Regarding the radiative properties of MBFs, we find as follows: (a) for each spectral type considered here, the magnetic model has always a higher mean intensity and a higher radiative flux than the corresponding non-magnetic model. The solar magnetic model (G2V) has the largest surplus in intensity and flux. (b) The surplus in radiative flux of the magnetic over the non-magnetic models, $\delta_{F_{\rm bol}}$ always exceeds that of the intensity of the vertically propagating radiation, $\delta_{I_{\rm bol}}$. (c) The difference $\delta_{F_{\rm bol}} - \delta_{I_{\rm bol}}$ monotonically increases with increasing effective temperature, owing to the monotonically increasing WD and degree of evacuation. (d) At disk center, MBFs of spectral type K8V and G2V are equally bright as granules. Model K2V shows MBFs that are 14.2% brighter than average granules. The MBFs of spectral type F5V, on the other hand, are 6.2% darker than the average granules of F5V, which explains the decline of the radiative surpluses for stars warmer than the Sun despite the increasing WD.

The result of item a) was already found in the preliminary study of Steiner et al. (2014) for the same spectral type sequence and by Beeck et al. (2015b) for an even wider range of spectral types and initial field strengths. But for the solar model this is in disagreement with the results of Thaler & Spruit (2014) who found a radiative deficiency instead of surplus. The reason for this discrepancy remains to date an open issue.

For mean magnetic flux densities up to 50 G, we expect the small-scale magnetism of solar-like stars in the spectral range from F5V to K8V to produce a positive contribution to their bolometric luminosity. The modulation seems to be most effective for early G-type stars.

Acknowledgements. We are thankful to F. Calvo for valuable technical support. We also thank the referee for the enthusiastic and encouraging report with various comments that greatly helped improve the manuscript.

References

Atroshchenko, I. N., Gadun, A. S., & Kostyk, R. I. 1989a, Astrofizika, 31, 281
Atroshchenko, I. N., Gadun, A. S., & Kostyk, R. I. 1989b, in Solar and Stellar Granulation, eds. R. J. Rutten, & G. Severino, NATO ASIC Proc., 263, 521
Bastien, F. A., Stassun, K. G., Basri, G., & Pepper, J. 2013, Nature, 500, 427
Beeck, B., Schüssler, M., & Reiners, A. 2011, in 16th Cambridge Workshop on Cool Stars, Stellar Systems, and the Sun, eds. C. Johns-Krull, M. K. Browning, & A. A. West, ASP Conf. Ser., 448, 1071
Beeck, B., Cameron, R. H., Reiners, A., & Schüssler, M. 2013a, A&A, 558, A48
Beeck, B., Cameron, R. H., Reiners, A., & Schüssler, M. 2013b, A&A, 558, A49
Beeck, B., Schüssler, M., Cameron, R. H., & Reiners, A. 2015a, A&A, 581, A42
Beeck, B., Schüssler, M., Cameron, R. H., & Reiners, A. 2015b, A&A, 581, A43
Calvo, F., Steiner, O., & Freytag, B. 2016, A&A, 596, A43
Danilovic, S., Gandorfer, A., Lagg, A., et al. 2008, A&A, 484, L17
Davis, P. J., & Polonsky, I. 1972, in Handbook of Mathematical Functions, eds. M. Abramowitz, & I. A. Stegun (New York: Dover Publications), 877
Donati, J.-F., & Landstreet, J. D. 2009, ARA&A, 47, 333
Dravins, D., & Nordlund, Å. 1990a, A&A, 228, 203
Dravins, D., & Nordlund, Å. 1990b, A&A, 228, 184
Dunn, R. B., & Zirker, J. B. 1973, Sol. Phys., 33, 281
Faurobert-Scholl, M. 1993, A&A, 268, 765
Freytag, B. 2013, Mem. Soc. Astron. It. Suppl., 24, 26
Freytag, B., Steffen, M., Ludwig, H.-G., et al. 2012, JCP, 231, 919
Fröhlich, C. 2013, Space Sci. Rev., 176, 237
Giampapa, M. S. 2016, Asian J. Phys., 25
Gray, R., & Corbally, C. 2008, Stellar Specral Classification (Princeton: Princeton University Press)
Gustafsson, B., Edvardsson, B., Eriksson, K., et al. 2008, A&A, 486, 951
Harten, A., Lax, P. D., & van Leer, B. 1983, SIAM Rev., 25, 35
Haywood, R. D., Collier Cameron, A., Unruh, Y. C., et al. 2016, MNRAS, 457, 3637
Kochukhov, O., Petit, P., Strassmeier, K. G., et al. 2017, Astron. Nachr., 338, 428
Lockwood, G. W., Skiff, B. A., Henry, G. W., et al. 2007, ApJS, 171, 260
Ludwig, H.-G. 2006, A&A, 445, 661
Ludwig, H.-G., & Steffen, M. 2016, Astron. Nachr., 337, 844
Ludwig, H.-G., Freytag, B., & Steffen, M. 1999, A&A, 346, 111
Ludwig, H.-G., Allard, F., & Hauschildt, P. H. 2002, A&A, 395, 99
Ludwig, H.-G., Caffau, E., Steffen, M., et al. 2009, Mem. Soc. Astron. It., 80, 711
Magic, Z., Collet, R., Asplund, M., et al. 2013a, A&A, 557, A26
Magic, Z., Collet, R., Hayek, W., & Asplund, M. 2013b, A&A, 560, A8
Meunier, N., Lagrange, A.-M., & Desort, M. 2010, A&A, 519, A66
Mihalas, D. 1978, Stellar Atmospheres, 2nd edn. (San Francisco: W. H. Freeman and Co.)
Nordlund, Å., & Dravins, D. 1990, A&A, 228, 155
Pagano, I., Ayres, T. R., Lanzafame, A. C., et al. 2006, Ap&SS, 303, 17
Parker, E. N. 1978, ApJ, 221, 368
Rajaguru, S., Kurucz, R., & Hasan, S. 2002, ApJ, 565, 101
Reiners, A. 2012, Liv. Rev. Sol. Phys., 9, 1
Riethmüller, T. L., Solanki, S. K., Martínez Pillet, V., et al. 2010, ApJ, 723, L169
Shapiro, A. I., Solanki, S. K., Krivova, N. A., Yeo, K. L., & Schmutz, W. K. 2016, A&A, 589, A46
Spruit, H. C. 1976, Sol. Phys., 50, 269
Spruit, H. C. 1977, Sol. Phys., 55, 3
Spruit, H. C. 1979, Sol. Phys., 61, 63
Spruit, H. C., & Zweibel, E. G. 1979, Sol. Phys., 62, 15
Steiner, O. 2003, A&A, 406, 1083
Steiner, O. 2005, A&A, 430, 691
Steiner, O., Pneuman, G. W., & Stenflo, J. O. 1986, A&A, 170, 126
Steiner, O., Rajaguru, S. P., Vigeesh, G., et al. 2013, Mem. Soc. Astron. It. Suppl., 24, 100
Steiner, O., Salhab, R., Freytag, B., et al. 2014, PASJ, 66, 5
Tanner, J. D., Basu, S., & Demarque, P. 2013, ApJ, 767, 78
Thaler, I., & Spruit, H. C. 2014, A&A, 566, A11
Trampedach, R., Asplund, M., Collet, R., Nordlund, Å., & Stein, R. F. 2013, ApJ, 769, 18
Tremblay, P.-E., Ludwig, H.-G., Freytag, B., Steffen, M., & Caffau, E. 2013, A&A, 557, A7
Trujillo Bueno, J., Shchukina, N., & Asensio Ramos A. 2004, Nature, 430, 326
Vögler, A., Shelyag, S., Schüssler, M., et al. 2005, A&A, 429, 335
Webb, A. R., & Roberts, B. 1978, Sol. Phys., 59, 249
Wedemeyer-Böhm, S., & Rouppe van der Voort, L. 2009, A&A, 503, 225
Wiehr, E., Bovelet, B., & Hirzberger, J. 2004, A&A, 422, L63
Wu, K., Otoo, E., & Suzuki, K. 2009, Pattern Anal. Appl., 12, 117

Appendix A: $I_{\rm bol}(t)$ and $F_{\rm bol}(t)$ of the stellar models

Figure A.1 shows the bolometric intensity (*left*) and bolometric radiative flux (*right*) as a function of time for models F5V, K2V, and K8V from top to bottom, respectively.

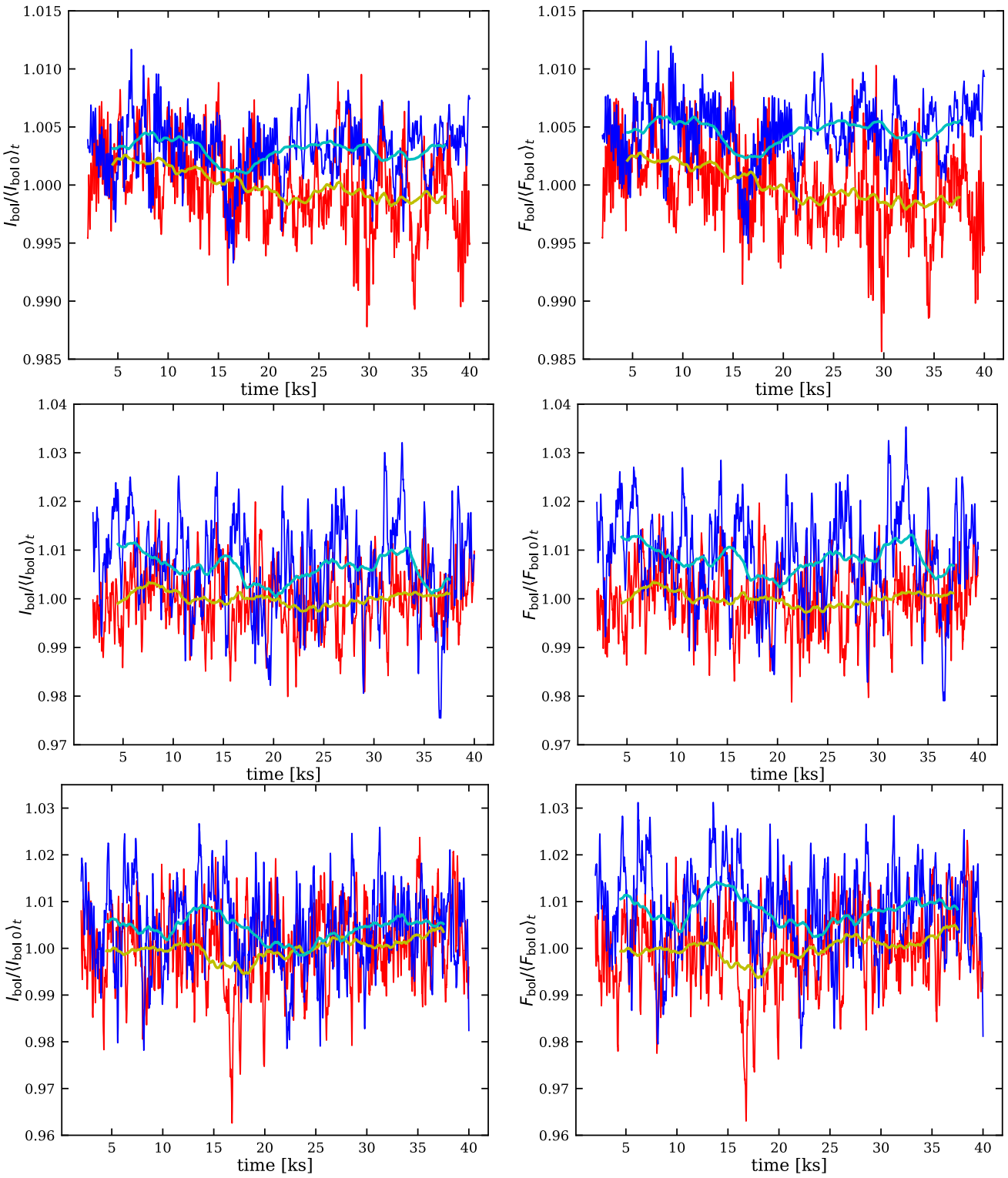

Fig. A.1. Bolometric radiative intensity (*left*) and bolometric radiative flux (*right*) leaving the computational domain in the vertical direction through the top boundary as a function of time for both the magnetic (blue curve) and the non-magnetic (red curve) models. From *top* to *bottom*: models K8V, K2V, and F5V. The cyan and orange curves are the moving (box car) average of the magnetic and non-magnetic model, respectively, with a time window width of 5000 s.

Appendix B: Counting of MBFs

In the present work, the magnetic filigree is defined as the area where the absolute value of the vertical component of the magnetic field, $|B_z(z_0)| > 1000\,\mathrm{G}$ at the spatial and temporal mean height of Rosseland optical depth $\tau_\mathrm{R} = 1$, i.e., at $z_0 = \langle z(\tau_\mathrm{R} = 1)\rangle$. We refer to this as the magnetic mask in Sect. 4. To establish the histogram for the WD in Fig. 9, we need to count the individual MBFs, which is carried out by performing a connected-component labeling as, for example, in Wu et al. (2009). With this algorithm, cells that are connected to each other within the magnetic mask are given the same label. Thus, cells with a common label constitute a single MBF and the labeling subdivides the filigree into individual MBFs. Thereby, the periodic side-boundary conditions must be taken into account. However, we found that this procedure also includes very small areas that cannot be identified as MBF and are often found within granules. Therefore, magnetic features of an area smaller than 15 grid cells have been filtered out. To further remove the bias toward small MBFs, we include in Fig. 9 the area weighted histogram. We consider this a more adequate representation of the WD because larger MBFs have greater influence on the radiative properties of the models than smaller MBFs.